Thesis for the degree
Master of Science

Submitted to the Scientific Council of the
Weizmann Institute of Science
Rehovot, Israel

עבודת גמר (תזה) לתואר
מוסמך למדעים

מוגשת למועצה המדעית של
מכון ויצמן למדע
רחובות, ישראל

By
Amit Tulchinsky

מאת
עמית טולצ'ינסקי

חקר של על-מוליכות טופולוגית במערכות ממימד נמוך
A Study of Topological Superconductivity in Low Dimensional Systems

Advisors:
Prof. Yuval Oreg
Prof. Ady Stern

מנחים:
פרופ' יובל אורג
פרופ' עדי שטרן

April 2019

ניסן ה'תשע"ט

Abstract

Two different low dimension systems were studied in this work, being candidates for exhibiting topological superconductivity. The first was an experiment-oriented study of a scanning tunneling microscope probe of a one dimensional (1D) system composed of a semiconducting InAs nanowire coated with superconducting Al islands.

It was found that a $\rho(E)$ model, in which the environment of the tunneling junction is described by a constant capacitance due to significant charging energy, describes the Coulomb blockade physics appearing in the conductance measurements rather well. To obtain an agreement with additional fine features in the conductance measurements we refined the environment model to include the effects of the interface between the island and the nanowire. The model we developed was also used to predict the effect of both regular and topological superconductivity on conductance measurements, which in the superconducting case was confirmed by measurements.

The second topic of study was a two dimensional (2D) system based on a model for a Chern insulator, but with introduced superconductivity. The precursor model was studied first as a baseline for the more advanced model, characterizing its topological phase diagram using the Chern number topological invariant of the system while laying down a general approach to calculate the topological invariant and the phase boundaries. This approach was utilized in the full model, after superconductivity was introduced in a simple intra-site form, to draw the phase diagram using the Chern number. The concept of weak topological phases was then introduced into our model, introducing two indices $\nu_{x,\pi}, \nu_{y,\pi}$ which together with ν fully characterize the topological phases and their corresponding edge mode structure. A complete topological phase diagram and a detailed account of the edge mode structure of the existing phases was then constructed. Finally, the conclusions were generalized to the case of additional, e.g. inter-site, weak superconducting pairings.

Contents

1 Table of Abbreviations

- SC - Superconductor\Superconductivity
- W.r.t. - With respect to
- STM - Scanning Tunneling Microscope
- DoS - Density of States
- DBTJ - Double-barrier Tunnel Junction
- nD - n-Dimensional
- BZ - 1st Brillouin Zone
- BHZ - Bernevig-Hughes-Zhang
- BdG - Bogoliubov-de Gennes

2 Introduction

Topological phases of matter, specifically topological insulators and topological superconductors, have garnered much attention in the past few years [1, 2, 3]. These phases of condensed matter systems are characterized by a band structure with a gap for bulk excitations and boundaries supporting topologically protected (robust against local perturbations) gapless edge states. In addition, topological defects in these phases may carry exotic zero-energy excitations with a similar topological protection. In topological superconductors, these defects usually come in the form of vortices in 2D superconductors with chiral symmetry and p-wave superconducting (SC) pairing [4] or edges of 1D spinless p-wave superconducting wires [5], and support localized states known as Majorana zero modes. Due to the non-Abelian exchange statistics of these zero modes, they have been proposed as possible ingredients for a topological quantum computer [6, 7], which makes them highly sought-after. This makes designing and studying realistic systems where Majorana zero modes appear an important theoretical issue. Most of the theoretical proposals for such systems exhibiting Majorana fermions are based on the above two low-dimensional models (1D spinless p-wave and 2D chiral p-wave superconductors) [8], and two specific ones will be at the focus of this thesis.

The first and currently the most promising and feasible experimental proposal for realizing Majorana zero modes devices is the quasi-1D semiconducting nanowire with strong spin-orbit coupling such as InAs or InSb, proximity coupled to an s-wave superconductor [9, 10]. Majorana zero mode signatures have been detected in recent experiments in heterostructures of such semiconducting wires and superconductors [11, 12]. A major barrier to advance such systems to handle dedicated quantum computation applications, however, is dubbed "quasiparticle poisoning" - processes that disturb the computation by changing the number of electrons in the system, since the ground state parity must be conserved for the topological protection to hold. A possible remedy to this problem is a suggested system design based on weakly coupled "Majorana islands", where the electrostatic charging energy E_C, which sets the energy scale for electron transport through the island, is large enough to prevent such transport and therefore fixes the total number of electrons in the system [13, 14]. In this realization, it is evident that the electronic properties of the buried interface between the semiconducting nanowire and superconducting islands must also be well understood before a device can be realized.

The second proposal involves reaching a realization of a spinless, chiral p-wave superconductor phase with a gapless edge state which is a chiral Majorana zero mode. A plethora of such possible realizations have been presented and studied, from a 2D spinless "p+ip"-pairing superconductor [4] to an array of weakly coupled p-wave superconductor nanowires [15], as well as many others [8, 16, 17]. Using a simple spinless model, an even more general analysis of the "topological class" of 2D chiral superconductors was performed, revealing a rich phase diagram as well as pointing out the role different types of topological invariants have in protecting the Majorana zero modes [18]. The "topological class" of a system refers to its place in the complete classification of topological phases based on its symmetries (time reversal, particle-hole, and chiral symmetries) and its dimensionality, and the different topological classifications are readily summarized in a type of "periodic table" [19, 20]. The spinless p-wave superconductor belongs to class D (particle-hole symmetric but not time reversal symmetric) and is characterized by a $\mathbb{Z}$ (integer) topological invariant which counts the number of gapless chiral Majorana modes on the system's boundary and differentiates between phases. When translational symmetry is also present, two additional $\mathbb{Z}_2$ topological invariants which count the parity of the number of chiral Majorana modes propagating in each direction can be defined. The $\mathbb{Z}$ invariant is referred to as a strong index, and the $\mathbb{Z}_2$ invariants as weak indices [21]. These afford a more

comprehensive description of the topological phases of the system and the existing edge modes.

This work set out to further push the boundary on both the study of realizable topological superconductors from a more experimental approach and the study of new theoretical models for possible rich and novel realizations of a topological superconducting phase with Majorana zero modes and Majorana edge modes.

The thesis outline is as follows: in Chapter 3, a theoretical study of an experimental scanning tunneling microscope (STM) probe of the "Majorana island" realization detailed above is brought forth, done in collaboration with experimentalist Dr. Jonathan Reiner (who performed the experiment and collaborated on the analysis) of Dr. Haim Beidenkopf's group. The experimental setup is described and then the suggested theoretical treatment of the system and its implications is detailed, closely following each step by supporting evidence - numerical simulation of the theoretical model fitted to the experimental measurements. We start by attempting to understand the system when no superconductivity is present, and finish by tackling superconductivity, specifically seeking to pinpoint the signature of topological superconductivity (if it exists) in such a system.

In Chapter 4, we suggest a new topological class D model which is based on a Chern insulator, a class A (no symmetries) topological insulator, with introduced superconductivity. We first study the phase diagram of the Chern insulator, proceed to introduce superconductivity in the simplest possible form, continue on to build the topological phase diagram and characterize the system's strong and weak topological phases and edge modes, and finish by discussing the most general manner in which superconductivity can be introduced to the system.

Finally, in Chapter 5 we conclude and propose interesting future directions for research.

3 Topological Superconductivity Signature in a 1D System: An STM probe of Al-coated InAs Nanowires

3.1 The Experimental Setup and the Scanning Tunneling Microscope

The experimental approach was a low-temperature scanning tunneling microscopy (STM) probe of a material system of the type described in the introduction - InAs (semiconductor) nanowires epitaxially coated with Al (a superconductor with a bulk critical temperature $T_C = 1.2$ K) islands, as can be seen in Figure (1).

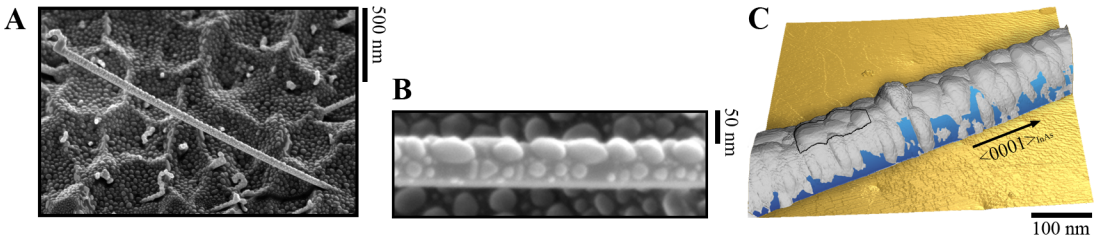

Figure 1: (A-B) Scanning Electron Microscope image of an InAs nanowire covered with epitaxially grown Al islands. **(C)** False-color STM topography of a nanowire (blue) on a gold substrate (yellow) covered with Al islands (gray). The effective shape of the tip apex smears the islands so that the Al cover appears continuous. The arrow label denotes the InAs crystallographic axis.

An STM measurement is based on an atomically sharp conducting tip positioned a very short distance from the surface of a sample, forming a tunnel junction - a system comprised of two conducting materials we label "electrodes" (in this case the STM tip and the sample), separated by a potential barrier (the vacuum\air between the two), where the electrons from an electrode can only move to the other electrode via quantum tunneling through the barrier. Using a semiclassical model of single-electron stochastic tunneling [22], the tunneling rate of electrons from electrode a through the junction to electrode b is then given by a Fermi Golden Rule calculation [23, 24] (assuming that the quantum probabilities for elastic tunneling of electrons in different energy levels are independent, and therefore the net transition rate can be calculated by integrating over the single-electron energy levels):

$$\Gamma_{ab} = \frac{2\pi}{\hbar}\int_{-\infty}^{\infty} |T_{ab}(E)|^2 \rho_a\left(E-\varepsilon_{\mathrm{F}}^a\right)\rho_b\left(E-\varepsilon_{\mathrm{F}}^b\right) f\left(E-\varepsilon_{\mathrm{F}}^a\right)\left(1-f\left(E-\varepsilon_{\mathrm{F}}^b\right)\right) dE. \tag{1}$$

Where $T_{ab}(E)$ is the tunneling matrix element (which is determined by the overlap of the wavefunctions from both conductors as well as the properties of the barrier), $\rho_i(E)$ is the local electronic density of states (DoS - the number of electronic states per unit energy) at electrode $i = a, b$, $\varepsilon_{\mathrm{F}}^i$ is the Fermi energy of electrode i and $f(E)$ is the Fermi-Dirac distribution function

$$f(E) = \frac{1}{e^{\frac{E}{k_{\mathrm{B}}T}}+1}, \tag{2}$$

where k_{B} is the Boltzmann constant and T is the temperature (it is assumed all components of the system are at thermal equilibrium). We note that all the integrands are generally energy dependent.

The energy difference $\varepsilon_{\mathrm{F}}^b - \varepsilon_{\mathrm{F}}^a$ is just the energy an electron gains during the tunneling event (from a to b). Assuming that the charge distribution completely relaxes during the tunneling event (the time of tunneling

is much longer than the relaxation time of the system but shorter than the time between tunneling events), the energy difference is given by the change in the electrostatic energy of the system [23]. When applying an external voltage bias V over the junction, this energy difference is just eV, with e being the electron charge. For a graphic depiction, see Figure (2).

The STM apparatus is constructed so that the density of states of the metallic tip around ε_{F} changes on an energy scale sufficiently larger than the energy scales considered, allowing it to be treated as uniform, and the tip is kept at such a distance from the sample as to make the overlap between the wavefunctions of electrons at electrodes a and b exponentially small, allowing us to use the Bardeen approximation - under reasonable assumptions on the wavefunctions, we treat $T(E)$ as virtually independent of the energy difference $\varepsilon_{\mathrm{F}}^{b} - \varepsilon_{\mathrm{F}}^{a}$, depending instead only on the distance between the tip and the sample s [25]:

$$|T_{ab}(E)|^2 \equiv |M|^2 = e^{-2\kappa s}, \tag{3}$$

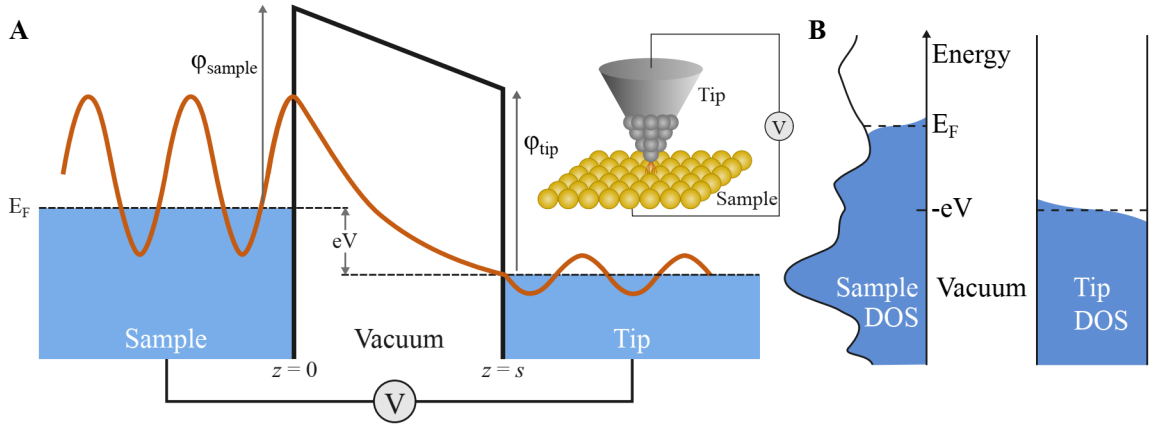

Figure 2: **(A)** Schematic diagram of a tunnel barrier with two metallic electrodes. The electrodes are separated by a thin vacuum barrier and biased by voltage V. The respective barrier height is $\varphi_{\mathrm{sample}}$ and φ_{tip}. The tunneling current is facilitated by the exponential tails of the wavefunctions. Inset: The STM realization of the tunneling barrier. **(B)** Energy diagram of the respective DoS of the tip (assumed to be flat) and the sample. The curves in the lateral direction correspond to total DoS at the corresponding energy, while blue signifies filled states. Only electrons in the range $[\varepsilon_{\mathrm{F}}, \varepsilon_{\mathrm{F}} \pm eV]$ contribute to the tunneling current (up to thermal broadening). Figure taken from [26].

where $\kappa \sim 1\mathring{A}^{-1}$, causing an exponential decline in amplitude on an atomic scale, the key feature behind the STM's ability to create sample topography maps at atomic-scale resolution (see Figure (1)C).

The overall tunneling current from the tip to the sample is just:

$$I = e\left(\Gamma_{\mathrm{tip}\to\mathrm{sample}} - \Gamma_{\mathrm{sample}\to\mathrm{tip}}\right). \tag{4}$$

Aggregating the above results and assumptions, as well as assuming the temperature energy scale $k_B T$ to be smaller than all relevant energy scales and so can be treated as 0, one arrives at a clean expression for the tunneling current:

$$I(V) = -\frac{4\pi e}{\hbar}\rho_{\mathrm{tip}}(0)\,|M|^2 \int_{-eV}^{0} \rho_{\mathrm{sample}}(\varepsilon_{\mathrm{F}} + \epsilon)\, d\epsilon. \tag{5}$$

This means that around any bias V a differential conductance measurement will yield:

$$\frac{dI}{dV}|_V \propto \rho_{sample}\left(\varepsilon_{\mathrm{F}} - eV\right), \tag{6}$$

allowing a probing of the energy dependence of the local density of states of the sample. Moreover, by varying the distance between tip and sample such that $\frac{dI}{dV}$ is locked at some predetermined value (assuming ρ_{sample} changes little along the sample edge), a topographical map of the sample surface is obtained.

For the sake of consistency, we note that the way $\frac{dI}{dV}$ is measured (creating an AC voltage oscillation with amplitude dV around the DC voltage V and measuring the resulting current modulation dI) introduces an instrumental error ~ 5 meV (comparable to the error introduced by a temperature of about ~ 50 Kelvin) to the measurement which is an order of magnitude larger than the error$\sim 1 - 0.1$ meV obtained from neglecting the temperature in the experiment $(0.4 - 4.2$ K) or less, mildly supporting our previous neglect of temperature effects regardless of the electronic energy scales in the problem.

3.2 The $\rho(E)$ Model

In most settings such an STM probe is enough to determine the sample DoS. Indeed, differential conductance measurements in uncoated areas of the nanowire are almost identical to such measurements on a completely uncoated nanowire, and both correspond to the predicted density of states of a 1D semiconductor system as can be seen in Figure (3) when compared to Appendix (7.1).

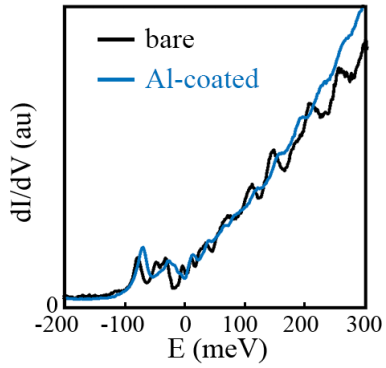

Figure 3: Typical conductance ($\frac{dI}{dV}$) curves measured for a bare nanowire (black) and for a nanowire coated with Al islands (blue, where the measurement was done off the islands). In both cases the conduction band begins at about the same energy - 100 meV below $\varepsilon_{\mathrm{F}}^{\mathrm{tip}}$.

However, measurements over the Al droplets are not reminiscent of the flat (metallic) Al DoS, the nanowire DoS or any simple superposition of the two. This (and further spectral features which we will tackle later on) lead to the understanding that electrons that cross the Al to InAs interface encounter an energy barrier, and the Al droplet to nanowire interface actually acts as a second tunnel junction (the STM tip to droplet interface being the first), with the complete system now a double-barrier tunnel junction (DBTJ).

DBTJ systems have been theoretically studied in simplified settings, and modeled successfully by a simplified $\rho(E)$ model of correlated electron tunneling [24, 27], with an analytical solution even for a more general setting [23]. This model assumes:

1. The semiclassical assumption: The state of the DBTJ is fully determined by a single classical variable

V, the voltage over the junction. Moreover, the the tunneling current is given by equation (1) with the same underlying assumptions, and is determined fully by electrostatic energy considerations over the junction:

$$\varepsilon_{\mathrm{F}}^{a} - \varepsilon_{\mathrm{F}}^{b} \equiv -\Delta E_{ab}. \tag{7}$$

2. Each tunneling junction i is a mesoscopic component: It has a finite capacitance C_i and resistance R_i, such that the consequent charging energies (the energy required to charge the junction with one elementary charge e) $E_{C_i} \equiv \frac{e^2}{2C_i}$ is greater than the thermal energy of the system $E_{C_i} > k_{\mathrm{B}}T$ and also $R_i > R_{\mathrm{Q}}$ where $R_{\mathrm{Q}} \equiv \frac{\pi\hbar}{2e^2} \sim 6.5\ \mathrm{k}\Omega$ is the resistance quantum. The DBTJ is represented in terms of a classical circuit as demonstrated in Figure (4).

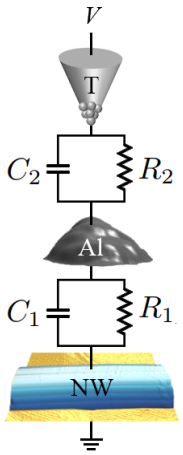

Figure 4: Schematic diagram of the equivalent classical circuit to the DBTJ system when the STM tip is positioned over an Al droplet. Junction 1 corresponds to the Al island-nanowire interface while junction 2 corresponds to the STM tip-Al island interfact. The nanowire is grounded (zero voltage) while the tip is gated (voltage V).

As the tunneling process is also assumed stochastic, the number of extra electrons N on the island resulting from a tunneling process at any time t is modeled by a probability distribution function $\sigma(N, V, t)$ (where, following the assumption, this probability is fully determined by V). As we are interested in a steady state solution, the t dependence can be discarded and $\sigma(N, V)$ must satisfy a detailed balance relation, requiring the net probability for making a transition between any two adjacent states in a steady state to be zero:

$$\sigma(N,V) \underbrace{\left(\Gamma_{+}^{1}(N,V) + \Gamma_{+}^{2}(N,V)\right)}_{\substack{\text{total tunneling rate onto} \\ \text{island with } N \text{ electrons}}} = \underbrace{\left(\Gamma_{-}^{1}(N+1,V) + \Gamma_{-}^{2}(N+1,V)\right)}_{\substack{\text{total tunneling rate out of} \\ \text{island with } N+1 \text{ electrons}}} \sigma(N+1,V). \tag{8}$$

Where $1, 2$ denote the island-nanowire junction and the tip-island junction respectively, and $+$ $(-)$ signify tunneling onto (off) the island. A normalization of probability constraint must also be present for any V:

$$\sum_{N=-\infty}^{\infty} \sigma(N,V) = 1. \tag{9}$$

An analytical solution for $\sigma(N,V)$ solely in terms of the tunneling rates $\Gamma_j^{\pm}(N,V)$ exists [23]:

$$\sigma(N,V)=\frac{\prod_{i=-\infty}^{N-1}\left(\Gamma_+^1(i,V)+\Gamma_+^2(i,V)\right)\prod_{i=N+1}^{\infty}\left(\Gamma_-^1(i,V)+\Gamma_-^2(i,V)\right)}{\sum_{j=-\infty}^{\infty}\left[\prod_{i=-\infty}^{j-1}\left(\Gamma_+^1(i,V)+\Gamma_+^2(i,V)\right)\prod_{i=j+1}^{\infty}\left(\Gamma_-^1(i,V)+\Gamma_-^2(i,V)\right)\right]}. \tag{10}$$

Moreover, it is expected to be sharply peaked

Next, taking into account the energy change resulting from a single tunneling event using electrostatic circuit energy considerations, we have:

$$\begin{array}{ll}\Delta E_1^{\pm} & =\Delta U^{\pm}\pm\frac{eC_2}{C_1+C_2}V\\ \Delta E_2^{\pm} & =\Delta U^{\pm}\mp\frac{eC_1}{C_1+C_2}V\\ \Delta U^{\pm} & =\frac{(Q\pm e)^2}{2(C_1+C_2)}-\frac{Q^2}{2(C_1+C_2)},\end{array} \tag{11}$$

where Q is the excess charge on the center electrode before the tunneling event. $\Delta U^{\pm}$ is just the change in charging energy of the center electrode as it gains or loses one electron respectively, and the second term in $\Delta E_j^{\pm}$ is the potential difference across the corresponding junction times the electron charge. We denote $Q=Ne-Q_0$, where N is the integer nearest $\frac{Q}{e}$ ($|Q_0|\leq\frac{e}{2}$) and Q_0 accounts for the possible presence of a fractional residual charge, which is thought to be due to the difference in the work functions of the different materials used in the junctions [28] and therefore remains unchanged with tunneling events (and as such is only a function of the location of the tip over the sample and not a function of N or V).

We can rewrite equations (11) as

$$\begin{array}{ll}\Delta E_1^{\pm} & =E_C\left(1+2\left(N-\frac{Q_0}{e}\right)\right)\pm\frac{eV}{1+\frac{C_1}{C_2}}\\ \Delta E_2^{\pm} & =E_C\left(1-2\left(N-\frac{Q_0}{e}\right)\right)\mp\frac{eV}{1+\frac{C_2}{C_1}},\end{array} \tag{12}$$

where $E_C\equiv\frac{e^2}{2(C_1+C_2)}$ is the DBTJ total charging energy. The tunneling rates are simple to determine in most realizations of the simplified $\rho(E)$ model - the tunneling matrix element is assumed independent of energy for both junctions ($T_{1,2}(E)\equiv T_{1,2}^0$) and the density of states for all electrodes is assumed to be metallic (constant in energy measured relative to their Fermi energy: $\rho_{\mathrm{tip}}(E)=\rho_{\mathrm{tip}}^0$, $\rho_{\mathrm{Al}}(E)=\rho_{\mathrm{Al}}^0$, $\rho_{\mathrm{InAs}}(E)=\rho_{\mathrm{InAs}}^0$), simplifying eq. (1) giving the simple form:

$$\Gamma_j^{\pm}(N,V)=\frac{-\Delta E_j^{\pm}}{R_j e^2}\Theta\left(-\Delta E_j^{\pm}\right), \tag{13}$$

where

$$R_j\equiv\frac{\hbar}{2\pi e^2}\frac{1}{\rho_{j,a}^0\rho_{j,b}^0\left|T_j^0\right|^2} \tag{14}$$

is appropriately recognized as the resistance of junction j ($\rho_{j,i}^0$ are the DoS of the two electrodes $i=a,b$ comprising junction j), Θ is the Heaviside step function and negligible temperature $T\ll\Delta E_j^{\pm}$ was assumed.

Finally, the current through the DBTJ is given by:

$$\begin{array}{ll}I(V) & =e\sum_{N=-\infty}^{\infty}\sigma(N,V)\left(\Gamma_2^+(N,V)-\Gamma_2^-(N,V)\right)\\ & =e\sum_{N=-\infty}^{\infty}\sigma(N,V)\left(\Gamma_1^-(N,V)-\Gamma_1^+(N,V)\right)\end{array} \tag{15}$$

and the differential conductance $\frac{dI}{dV}(V)$ is just the derivative of equation (15) with respect to (w.r.t.) V.

When used in the framework of standard STM measurements, the model can be greatly simplified by assuming $R_2 \gg R_1$, justified because the tip-sample resistance in such experiments is on the order of $1\text{G}\Omega$ contrasted with standard sample resistances on the order of $1-10\text{K}\Omega$. We dwell on this approximation and the simple $\rho(E)$ model because it affords insight on the broad-strokes behavior of the DBTJ.

First, by combining this assumption with equations (8),(13) it is evident that $\sigma(N,V)$ is sharply peaked around some most-probable number of electrons on the central electrode $N_0(V)$ ($\sigma(N,V) \approx \delta_{N,N_0(V)}$) which is set as the integer which satisfies

$$e^{-1}\left(-C_2V + Q_0 - \frac{e}{2}\right) \leq N_0 \leq e^{-1}\left(-C_2V + Q_0 + \frac{e}{2}\right) \tag{16}$$

and the current is given by

$$I(V) = \begin{cases} 0 & \frac{-\frac{e}{2}+N_0e-Q_0}{C_1} \leq V \leq \frac{\frac{e}{2}+N_0e-Q_0}{C_1} \\ \frac{-(N_0e-Q_0)+C_1V-\frac{e}{2}\text{sgn}(V)}{R_2(C_1+C_2)} & \text{else} \end{cases}. \tag{17}$$

A typical $\sigma(N,V)$ plot validating our sharply-peaked assumption and an $I(V)$ curve with its corresponding conductance ($\frac{dI}{dV}$) curve is given in Figure (5).

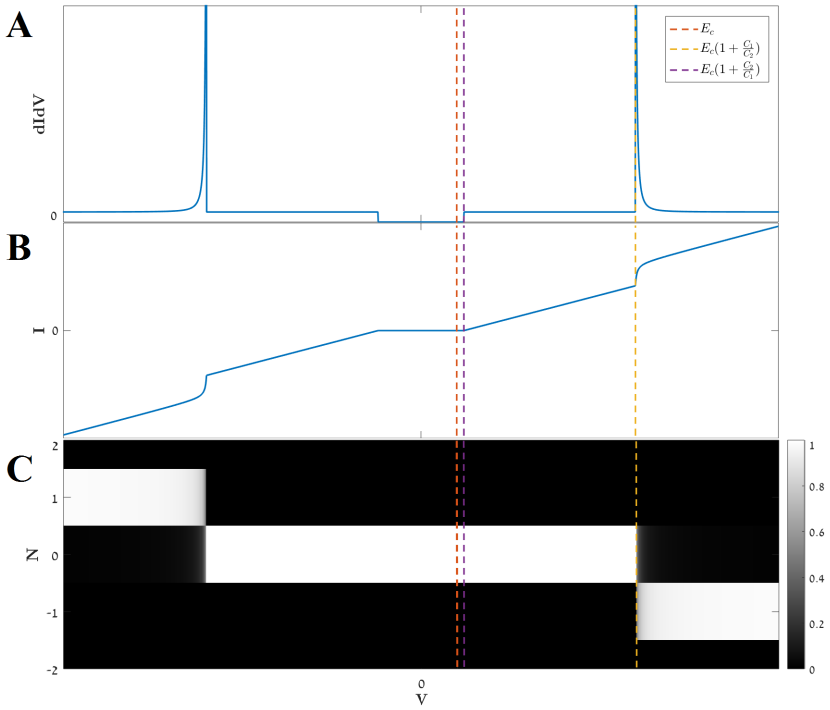

Figure 5: Typical curves for the simplified $\rho(E)$ model ($R_2 \gg R_1$, $C_2 < C_1$), simulated. Voltage is measured in units of energy (eV). Note the voltage scaling of the features derived from equations (16),(17) detailed in the legend. **(A)** Conductance ($\frac{dI}{dV}(V)$) curve. Note the presence of both the Coulomb gap and the charging resonances. **(B)** Corresponding current-voltage ($I(V)$) curve. **(C)** $\sigma(N,V)$ false color plot, describing the probability of electron occupation N at bias V.

The bias domain around $V = 0$ for which $I(V) = 0$ (and also $\frac{dI}{dV} = 0$) is dubbed the "Coulomb blockade" regime, where the electrostatic repulsion prevents electron transport through the island even when external voltage is applied, and the corresponding gap in the $\frac{dI}{dV}$ spectrum is labeled the "Coulomb gap".

At higher voltages the current enters a linear-in-V ("Ohmic") regime where

$$\begin{array}{rl} I(V) \propto & \left(R_2\left(1+\frac{C_1}{C_2}\right)\right)^{-1} V + \text{const.} \\ \frac{dI}{dV} = & \left(R_2\left(1+\frac{C_1}{C_2}\right)\right)^{-1} \end{array} \tag{18}$$

since it is energetically favorable for the system to allow electron transport through the island. This behavior is interrupted each time the bias affords enough energy for the electron occupation of the island N_0 to change by 1 (C_2V reaches the next integer multiple of $-e$), resulting in even more favorable conditions for electron transport through the island (leading to a discrete jump in $I(V)$ and therefore a sharp peak in conductance), after which the the Ohmic regime resumes (equation (18)), and so forth. As sharp peaks in the conductance curve signal a change in the island charge, they are labeled "charging resonances".

In order to isolate any effects non-pertinent to superconductivity that are not accounted for by the simplified $\rho(E)$ model, such as effects that the non-metallic nanowire might introduce, the first measurement of the experiment was performed at $T = 4.2$ K (above T_C). It turns out that the simplified $\rho(E)$ model accounts excellently for the broad-stroke features of the conductance measurements performed in this measurement as is shown by the dashed red line best fit in Figure (6). The Coulomb gap and charging resonances, as well as the overall behavior, comply with the model. An artificial Gaussian smearing is introduced to account for the finite resonance height and width (originates mostly from finite instrument accuracy, which is set as the Gaussian's σ parameter).

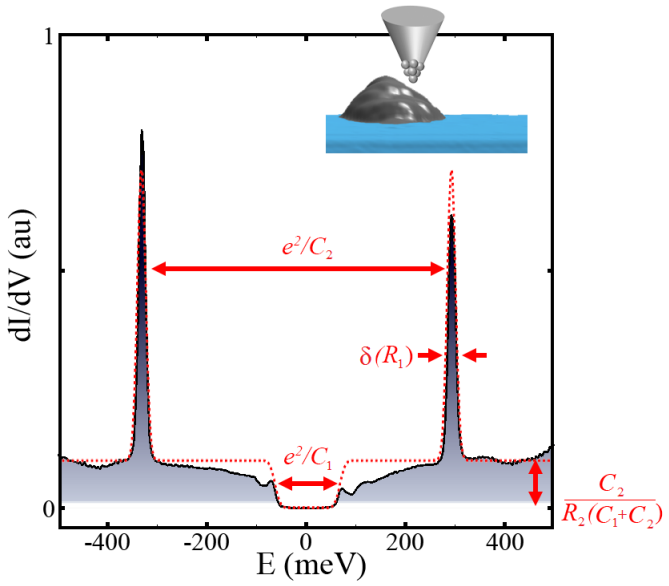

Figure 6: $\frac{dI}{dV}$ at a particular position on the droplet (inset) at $T > T_C$, with a fit to the simplified $\rho(E)$ model (red dashed line). The annotations refer to the circuit parameters that can be extracted from the measurement using equations (16),(17) and (19). Note the excellent fit of the model to the broad-stroke features (resonance peak location and width, Coulomb gap location) contrasted with its poor fit to the fine features mainly at the exit of the Coulomb gap.

This model also captures the asymmetry of the gap and peaks w.r.t. $V = 0$ via Q_0, which affects the conductance by shifting the Coulomb gap and the charging resonances in opposite directions in energy, explaining their anti-correlated shifts observed when the tip scans over the island (Q_0 is dependent, among

other things, on the work function close to the tip, and therefore changes as the droplet is scanned) as can be seen in Figure (7). Accounting for this from now on, we can disregard this effect henceforth.

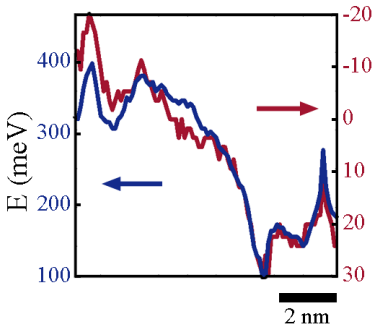

Figure 7: Positive resonance peak voltage (blue) and voltage measured at the middle of the Coulomb gap (red) as the tip scans over a droplet, illustrating their anti-correlated nature. Notice the opposite and scaled corresponding voltage axes. This anti-correlated shift is taken into account by the model parameter Q_0.

However, as can be seen in Figure (6), a notable deviation from the model occurs at the onset of the Ohmic-like regime, which exhibits a nontrivial structure that suggests additional physics we did not capture, and which will be discussed below.

Extracting C_1, C_2 and R_2 predicted by the model using the method described in Figure (6) gives $C_1 \sim 1.5$ aF, $C_2 \sim 0.3$ aF ($C_1 > C_2$) as well as $R_2 \sim 1$ GΩ (which fits our estimate from before). To estimate R_1, we note that the width of the resonance in Figure (6) is actually larger than the experimental resolution (taking into considering both temperature-induced broadening and instrumental broadening). This broadening δ around the charging peak V_p actually results from our crude approximation $\frac{R_1}{R_2} \approx 0$, and can be used to estimate R_1 via $\Gamma_1(V_\mathrm{p}) = \frac{V_\mathrm{p}}{eR_1\left(1+\frac{C_1}{C_2}\right)}$ and the time-energy uncertainty relation $\delta \sim \hbar\Gamma_1(V_\mathrm{p})$ [29], leading to:

$$R_1 \propto \frac{\hbar}{e}\left(1+\frac{C_1}{C_2}\right)^{-1}\frac{V_\mathrm{p}}{\delta}. \tag{19}$$

By measuring the conductance at multiple points on the island, one can extract C_1,C_2,V_p and δ and evaluate R_1 using equation (19). Surprisingly, it appears R_1 decreases with the peak energy $E = eV_\mathrm{p}$ as is evident in Figure (8), which suggests R_1 is an energy dependent quantity.

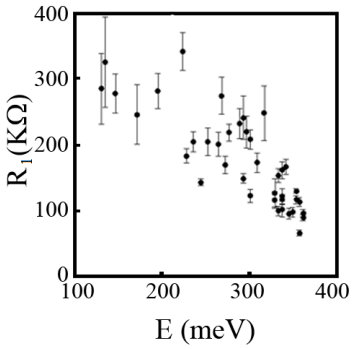

Figure 8: A plot of R_1 extracted using equation (19) from multiple conductance measurements, each having a different peak energy eV_{p}. It confirms that the island-nanowire resistance R_1 depends on the energy of the tunneling electrons, decreasing with E.

Equations (1), (13), (14) strengthen our aforementioned suspicion that some of the previous assumptions we made to construct the simplified $\rho(E)$ model are unjustified, and further focuses it to two particular challenges on our assumptions - the tunneling barrier at the island-nanowire interface being energy dependent (which leads to an energy dependent tunneling matrix element $T_1(E) \neq \text{const.}$) and the nontrivial nanowire DoS ($\rho_{\mathrm{InAs}}(E) \neq \text{const.}$). Moreover, we would like to account for a trivial\topological superconducting island, which would also imply nontrivial island DoS ($\rho_{\mathrm{Al}}(E) \neq \text{const.}$).

3.3 Refined $\rho(E)$ Model

It is at this point that we to turn to a less simplistic DBTJ description, which includes the nontrivial energy dependence of $\rho_{\mathrm{InAs}}(E)$,$T_1(E)$ and $\rho_{\mathrm{Al}}(E)$. Returning to equations (10), (15), we notice that the conductance is dependent only on the tunneling rates $\left\{\Gamma_j^{\pm}\right\}_{j=1,2}$ as they also uniquely determine $\sigma(N,V)$. Re-examining equation (1) with an appropriate change of variables, assuming $T=0$, using equation (7) and redefining $T(E)$ w.r.t. to $\varepsilon_{\mathrm{F}}^a$ (the Fermi energy of electrode a), we find the more general alternative to equation (13):

$$\Gamma_{ab} = \frac{2\pi}{\hbar}\Theta\left(-\Delta E_{ab}\right)\int_{\Delta E_{ab}}^{0} \left|T_{ab}(E)\right|^2 \rho_a(E)\,\rho_b\left(E-\Delta E_{ab}\right)dE \tag{20}$$

meaning essentially $\Gamma_{ab}(N,V) = \Gamma_{ab}\left(\Delta E_{ab}(N,V)\right)$. In this setting the "Ohmic" resistances R_j can be generalized to:

$$\begin{aligned}
R_1^{+}\left(\Delta E_1^{\pm}\right) &\equiv \frac{\hbar}{2\pi e^2}\frac{-\Delta E_1^{+}}{\int_0^{-\Delta E_1^{+}} |T_1(E)|^2 \rho_{\mathrm{Al}}(E)\rho_{\mathrm{InAs}}\left(E+\Delta E_1^{+}\right)dE} \\
R_1^{-}\left(\Delta E_1^{-}\right) &\equiv \frac{\hbar}{2\pi e^2}\frac{-\Delta E_1^{-}}{\int_{\Delta E_1^{-}}^{0} |T_1(E)|^2 \rho_{\mathrm{Al}}(E)\rho_{\mathrm{InAs}}\left(E-\Delta E_1^{-}\right)dE} \\
R_2^{+}\left(\Delta E_2^{+}\right) &\equiv \frac{\hbar}{2\pi e^2}\frac{-\Delta E_2^{+}}{\left|T_2^0\right|^2 \rho_{\mathrm{tip}}^0 \int_0^{-\Delta E_2^{+}} \rho_{\mathrm{Al}}(E)dE} \\
R_2^{-}\left(\Delta E_2^{-}\right) &\equiv \frac{\hbar}{2\pi e^2}\frac{-\Delta E_2^{-}}{\left|T_2^0\right|^2 \rho_{\mathrm{tip}}^0 \int_{\Delta E_2^{-}}^{0} \rho_{\mathrm{Al}}(E)dE},
\end{aligned} \tag{21}$$

where now

$$\Gamma_j^{\pm}\left(\Delta E_j^{\pm}\right) = \frac{-\Delta E_j^{\pm}}{R_j^{\pm}\left(\Delta E_j^{\pm}\right)e^2}\Theta\left(-\Delta E_j^{\pm}\right), \tag{22}$$

and we assumed the tunneling matrix element is independent of tunneling direction (+ or −).

Finally, using any functional forms of $T_1(E)$,$\rho_{\mathrm{InAs}}(E)$ and $\rho_{\mathrm{Al}}(E)$, we can now use equations (10), (21), (22) to solve for $\Gamma_j^{\pm}(N,V)$,$\sigma(N,V)$ for any N,V and from there use equation (15) to solve for $\frac{dI}{dV}$ for any V. This is generally not analytically solvable, and so a numerical simulation calculating the conductance $\frac{dI}{dV}(V)$ was written in MATLAB (for more details, see Appendix (7.2)) to enable further fitting of the fine features of the experimental data using functional forms for $T_1(E)$,$\rho_{\mathrm{InAs}}(E)$ and $\rho_{\mathrm{Al}}(E)$ which include fitting parameters (and the other fitting parameters described above).

3.3.1 Nontrivial Nanowire DoS

We strive to explain the conductance features of the first measurement, where superconductivity should be negligible ($T > T_{\mathrm{C}}$), and so we can treat the Al islands as metallic $\rho_{\mathrm{Al}}(E) = \text{const.}$, which means $R_2^+ = R_2^- \equiv R_2$ is again non-energy dependent and defined by equation (14) (and again we expect $R_2 \sim 1\ \mathrm{G\Omega}$). This means that we only need to account for the functional forms of $T_1(E)$ and $\rho_{\mathrm{InAs}}(E)$ before attempting to fit the data. In order to understand the compounded effect both nontrivial $T_1(E)$ and nontrivial $\rho_{\mathrm{InAs}}(E)$ have on the conductance, each was studied separately first.

In the first step, only nontrivial $\rho_{\mathrm{InAs}}(E)$ was assumed, with a theoretical model for the DoS of the nanowire (1D semiconductor) was constructed, where the boundaries for the fitting parameters of $\rho_{\mathrm{InAs}}(E)$ were determined by comparing it to the STM measurements of the nanowire as depicted in Figure (3) (for more details, see Appendix (7.1)). However, attempts to fit the island conductance data proved problematic - in the entire parameter domain the nontrivial $\rho_{\mathrm{InAs}}(E)$ creates an extreme asymmetry between positive and negative voltages in the conductance which is practically non-existent in the data, due to its own asymmetry in energy.

This implies that either the nanowire DoS changes considerably, or that some other effect dominates the fine conductance features enough to wipe out most of the features caused by the nontrivial nanowire DoS. This leads us to suspect that the nontrivial tunneling matrix element is behind the leading order effect we see in the conductance measurement, and so a nontrivial form for it was next considered, discarding this effect.

3.3.2 Nontrivial Tunneling Matrix Element

Next, only a nontrivial $T_1(E)$ was assumed. As it is symmetric in energy (equation (21)):

$$R_1(\varepsilon) \equiv R_1^+(\varepsilon) = R_1^-(\varepsilon) = \frac{\hbar}{2\pi e^2}\frac{-\varepsilon}{\rho_{\mathrm{Al}}^0\rho_{\mathrm{InAs}}^0\int_{\varepsilon}^{0}|T_1(E)|^2\,dE}. \tag{23}$$

Examining equations (10), (21) and (22), it is evident that for a given bias V, the dependence of the functional form of the conductance on the resistances is only through the ratio $\frac{R_1}{R_2}$ and not R_1, R_2 independently (up to a global scaling constant $\left(\frac{dI}{dV}\right)_0$ for $\frac{dI}{dV}(V)$ which depends on R_2, which we leave as a free fitting parameter anyway), which depends only on the form of the nontrivial DoS functions, tunneling matrix element and the capacitance values C_1, C_2.

Furthermore, we notice that the capacitances C_1, C_2 only come into play in the energy scaling (bias voltage scaling) of the problem as they appear only via $\Delta E_j^{\pm}$, where they scale all eV appearances by either $E_C\left(1+\frac{C_1}{C_2}\right)$ or $E_C\left(1+\left(\frac{C_1}{C_2}\right)^{-1}\right)$ (equation (12)). This scaling is also not affected by R_1, R_2 (additional energy scales can come in through the DoS functions or tunneling rate). This means that the capacitances generally only move the onset of features of the conductance around the voltage axis relative to one another

but do not introduce new features, and so could still be determined approximately using the previous simplified $\rho(E)$ model fit, as its description fits the general features of the conductance well. The ratio $\frac{R_1}{R_2}$ is determined for every V by the given functional form of $T_1(E)$.

As iterated before, the conventional assumption following Bardeen's tunneling theory is that the tunneling matrix element $T_1(E)$ is energy independent, or at the very least varying very little with energy [25], and therefore we expect the relation $\frac{R_1}{R_2} \ll 1$ to hold at all voltages. However, R_1 varies substantially (by a factor ~ 3) as a function of energy and is larger at energies close to the Coulomb gap (Figure (8)). We can reconcile this by the observation that Bardeen's theory considers only tunneling which occurs due to the overlap between exponentially vanishing tails of wavefunctions across a finite width of insulating barrier (the "weak coupling" limit). In our case, however, the tunneling barrier is formed over an atomically sharp epitaxial interface, leading instead to strong wavefunction hybridization. The resulting tunneling matrix element $T_1(E)$ should therefore generally depend strongly on the change in the wavefunctions' spatial form as a function of E. We also expect that in this setting $T_1(E) \overset{E\to 0}{=} 0$ - the argument for T_1 is measured w.r.t. $\varepsilon_{\mathrm{F}}^a - \varepsilon_{\mathrm{F}}^b$, meaning in this case $\varepsilon_{\mathrm{F}}^a = \varepsilon_{\mathrm{F}}^b$, and so no available states to tunnel into on both sides of the barrier, as they are filled up to the same Fermi energy and the tunneling is elastic. By the same reasoning, we also expect $|T_1(E)|^2$ to gradually increase with energy.

At the low V regime this implies $R_1 \propto \left(|T_1(\to 0)|^2\right)^{-1} \to \infty$ (equation (23)) and therefore R_1 should increase dramatically at low V, even to the extent of becoming comparable to or larger than R_2, in accordance with the measurements.

Understanding the effect a ratio $\frac{R_1}{R_2} \not\ll 1$ has on the conductance, specifically in the low V regime, is therefore critical. As was reasoned before, for fixed capacitances the features for a given V depend only on the ratio $\frac{R_1}{R_2}(V)$, up to a global scaling constant (a single one for all V). Therefore, it is possible and instructive to return to the framework of the simplified $\rho(E)$ model, where $\frac{R_1}{R_2} = \text{const.}$, and observe the effects such values of $\frac{R_1}{R_2}$ have in the low V regime, which should translate similarly to the actual low V regime of our system.

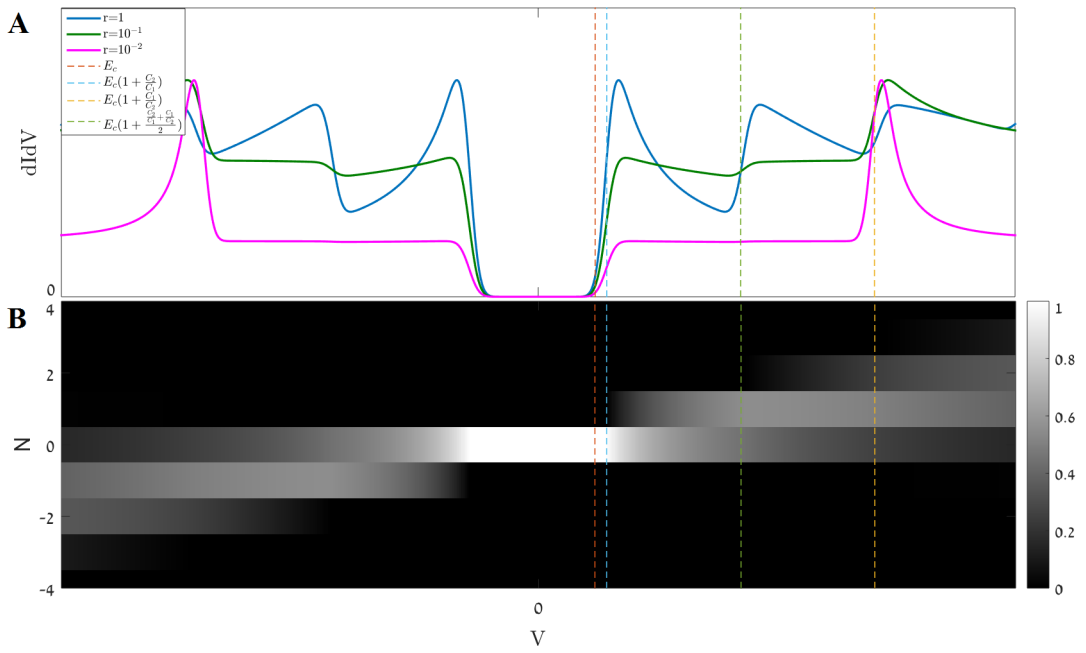

Figure 9: **(A)** Simulated conductance curves using the simplified $\rho(E)$ model (with the extracted values for the capacitances C_1, C_2) and varying resistance ratio $r \equiv \frac{R_1}{R_2} = \text{const.}$. As r approaches 1, in addition to the charging resonance at high energy (yellow dashed line) two new resonances emerge at the exit of the Coulomb gap (blue dashed line) and in between the two (green dashed line). **(B)** $\sigma(N, V)$ false color plot for the $r = 1$ case. Out of the Coulomb gap, there is now non-negligible probability for more than one N - the additional resonances can be explained by the probability for an additional island electron occupation N becoming possible at higher\lower V.

As can be seen in Figure (9), as $\frac{R_1}{R_2}$ increases in value up to the $\frac{R_1}{R_2} = 1$ case, two new resonances gradually emerge, one atop the exit of the Coulomb gap and the other between it and the original charging resonance. As the conductance data does contain a small resonance at the exit of the Coulomb gap (see Figure (6)), this indeed suggests that at the low V regime $T_1(E)$ is small enough such that $\frac{R_1}{R_2} \lesssim 1$, and that our reasoning above for its functional form is correct.

This leads us to suggest a simple model for the potential barrier at the atomically sharp epitaxial interface - a square potential barrier with an atomic scale width $w \approx 1 - 10\text{Å}$ and height V_0 (the work function). When solved, such a potential barrier leads to the functional form for the transmission [31]:

$$|T_1(E)|^2 = \begin{cases} \frac{1}{1+\frac{V_0^2 \sinh\left(\sqrt{\Phi(V_0-|E|)}\right)}{4|E|(V_0-|E|)}} & |E| \leq V_0 \\ \frac{1}{1+\frac{V_0^2 \sin\left(\sqrt{\Phi(|E|-V_0)}\right)}{4|E|(|E|-V_0)}} & |E| > V_0 \end{cases}, \tag{24}$$

where $\Phi = \frac{2m_*}{w^2\hbar^2}$ depends on the width of the barrier and the effective mass (here it is constrained $m_* \sim m_e - 0.01m_e$ where m_e is the bare electron mass).

The resulting best fit for the conductance in the low V regime presented in Figure (10) indeed captures the fine features identified in the measurement. It displays a peak at the exit of the Coulomb gap, indicating a transition to a regime of comparable resistances. The gradual increase in the conductance as V becomes larger therefore reflects the increase in $|T_1(E)|$, up to a constant value $|T_1(E)| \overset{E\to\infty}{\to} 1$, corresponding to the ratio $\frac{R_1}{R_2}$ going from ~ 1 to $\ll 1$, where the conductance goes to a constant value proportional to R_2^{-1}

(see equation (18)). In addition, our fitting corroborates the potential barrier width $w \sim 1$ nm and strength $V_0 \sim 0.5$ eV, meaning the presence of a sharp and substantial tunneling barrier is confirmed.

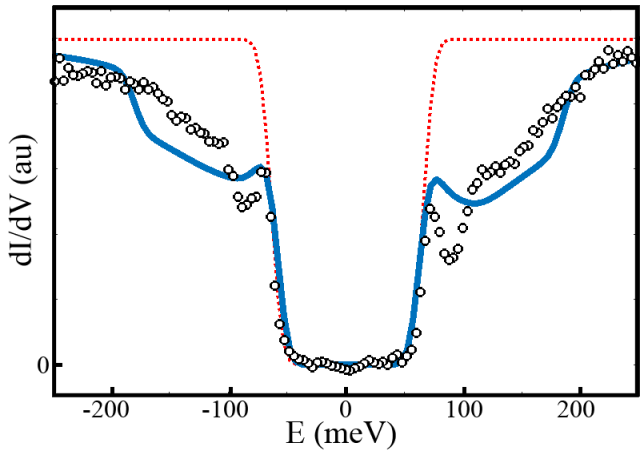

Figure 10: Low energy $\frac{dI}{dV}$ signal (circles) fitted with the simplified $\rho(E)$ model (red dotted line) and the refined $\rho(E)$ model that accounts for the energy-dependent transmission through the interface, $T_1(E)$ (solid line). Note the refined model accounts for the fine features at the exit of the Coulomb gap while the simplified model does not.

3.3.3 Theoretical Predictions for Superconductivity and Topological Superconductivity

After isolating the relevance of the nontrivial nanowire DoS and the nontrivial tunneling matrix element in the regime where the Al islands are not superconducting, the next step is to understand the isolated effect of superconducting and topological superconducting Al. For superconductivity, we take the Bardeen-Cooper-Schrieffer (BCS) theory DoS for a superconductor under its critical temperature $T < T_C$ in the zero temperature limit (consistent with our previous assumption) [30]:

$$\rho_{Al}^{SC}(E) = \rho_{Al}^{0} \frac{|E|}{\sqrt{E^2 - \Delta^2}} \Theta(|E| - \Delta) \tag{25}$$

Where ρ_{Al}^{0} is the DoS at the Fermi energy for the metallic phase and $\Delta \geq 0$ is the amplitude of the superconducting order parameter.

An additional even-odd effect which affects the electrostatic energy considerations is not expected to appear in the experiment due to the relatively high measurement temperature ($k_B T$ is larger than the level spacing in the Al island) and is therefore neglected [32, 33].

In order to account for topological superconductivity, the conventional signature associated with the Majorana zero energy state is included - a peak at zero energy [1, 10, 11, 12]. Accounting for this we get the DoS for a topological superconductor with n_{MZM} Majorana zero energy modes at zero temperature:

$$\rho_{Al}^{TSC}(E) = \rho_{Al}^{0} \frac{|E|}{\sqrt{E^2 - \Delta^2}} \Theta(|E| - \Delta) + n_{MZM} \delta(E). \tag{26}$$

The superconducting DoS introduces a new energy scale Δ. Solving for the tunneling rates using equations (21), (22) and (25) we find:

$$\Gamma_j^{\pm}(\Delta E_j^{\pm}) = \frac{1}{R_j} \Theta(-\Delta E_j^{\pm} - \Delta) \sqrt{(\Delta E_j^{\pm})^2 - \Delta^2}, \tag{27}$$

meaning the new condition for a nonzero tunneling rate $\Gamma_j^{\pm}$ therefore becomes $-\Delta E_j^{\pm} - \Delta > 0$, as opposed to the previous $-\Delta E_j^{\pm} > 0$. As at least one combination of rates Γ_1^+, Γ_2^- or Γ_1^-, Γ_2^+ must be nonzero for there to be nonzero current and therefore nonzero conductance through the DBTJ (else we just have charge accumulation on the island), using equation (12) and the observation that inside the gap $N = 0$, it becomes evident that the voltage to exit the gap is one of two voltages which correspond to the equations:

$$e\,|V| = \left(1 + \left(\frac{C_1}{C_2}\right)^{\pm 1}\right)\left(\Delta + E_C\left(1 \pm 2\frac{Q_0}{e}\right)\right). \tag{28}$$

The introduction of superconductivity therefore enlarges the gap V_{gap} from the previous Coulomb gap width

$$V_{\text{Coulomb}} = 2\frac{E_C}{e} \cdot \max_{\pm}\left\{1 + \left(\frac{C_1}{C_2}\right)^{\pm 1}\right\} \tag{29}$$

(notice Q_0 shifts the gap, but does not change its overall size, as previously mentioned) by an additive factor

$$V_{\text{SC}} = 2\frac{\Delta}{e} \cdot \max_{\pm}\left\{1 + \left(\frac{C_1}{C_2}\right)^{\pm 1}\right\} \tag{30}$$

to a total width $V_{\text{gap}} = V_{\text{Coulomb}} + V_{\text{SC}}$. This makes sense when considering that for both junctions we must first supply the system with enough voltage to reach occupied\available states at the exit of the SC gap Δ, and from there our treatment of the tunneling becomes similar to before.

We infer that this enhanced gap is expected to hold even in the presence of nontrivial nanowire DoS and tunneling matrix element, as these do not alleviate the problem of non-accessible states in the Al superconducting island. Experimental evidence supports this, as we have demonstrated above that the tunneling matrix element cannot be neglected, and still the system exhibits an enhanced gap (which is at least partially due to superconductivity, as it is susceptible to the introduction of a magnetic field) as can be seen in Figure (11).

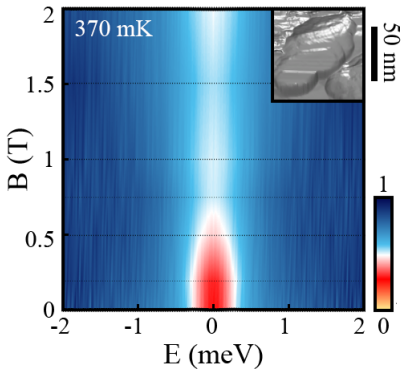

Figure 11: False color plot of conductance measurements performed at $T < T_C$ over a superconducting Al island (island shown in the inset) for different voltages (x axis) and magnetic fields (y axis). Colorbar represents normalized conductance (all conductance measurements are normalized so that the maximal conductance is 1). Measurements acquired at different magnetic fields (dashed lines) are interpolated to show the closure of the superconducting gap ($B \leq 0.5$T), leaving only the Coulomb gap ($B \geq 0.75$T).

The introduction of topological superconductivity just amounts to an addition $\delta\Gamma_j^{\pm}$ to all regular super-

conductivity tunneling rates $\Gamma_j^{\pm}$ (equations (26), (27)) of

$$\delta\Gamma_j^{\pm}\left(\Delta E_j^{\pm}\right) = \frac{1}{R_j}\frac{n_{\mathrm{MZM}}}{\rho_{\mathrm{Al}}^0}\Theta\left(-\Delta E_j^{\pm}\right), \tag{31}$$

which implies a constant (not voltage dependent) contribution to the tunneling rates for voltages that are larger than the Coulomb gap but smaller than the full superconductivity-induced gap. Also, the scaling of the voltages relevant to these terms is the same as in the no SC case (as Δ does not appear). This implies that the conductance signature of such Majorana zero energy modes first appears as a peak in sub-gap conductance at the onset of the Coulomb gap, shifted from zero bias by $\frac{1}{2}V_{\mathrm{Coulomb}}$, but also replicates periodically at additional multiples of the voltage scaling V_{Coulomb}, as can be seen in actual calculations in Figure (12).

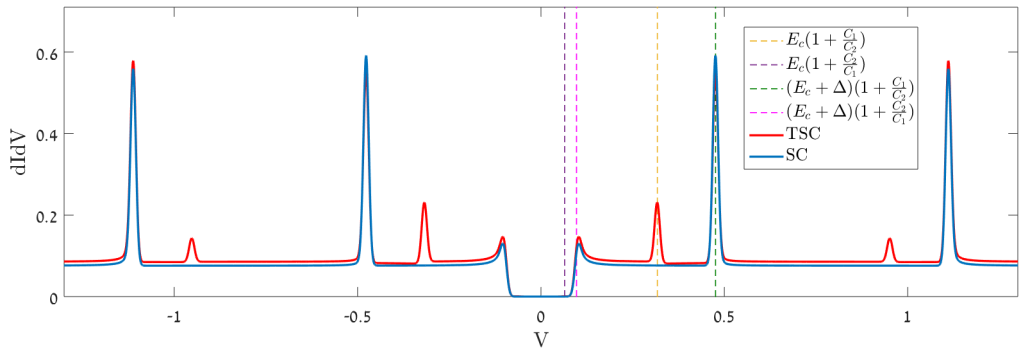

Figure 12: Simulated refined $\rho(E)$ model conductance for a trivial superconductor (red) and topological superconductor (blue). The charging resonances are shifted by the scaled $\Delta + E_C$ (pink, green dashed lines), while the zero energy peaks originating in the Majorana modes are shifted by the scaled E_C (purple, yellow dashed lines). The Majorana peak height is determined by the magnitude of n_{MZM}. Notice that the sub-gap Majorana peak is washed out by the finite measurement resolution, but the replicated peaks (appearing at $\frac{1}{2}V_{\mathrm{Coulomb}} + mV_{Coulomb}$ for integer m) are not.

This sharp, unique signature can be measured at multiple finite biases, making Majorana zero energy modes easier to resolve and distinguish from competing features in such conductance measurements. We emphasize that our model treats the Majorana zero modes only as a feature in the nanowire DoS, and therefore an accidental zero energy mode such as an Andreev bound state will yield similar results.

4 Topological Phases of a Chern Insulator-based 2D Topological Superconductor

As was stated in the introduction, in this part we suggest a new topological class D model which is based on a Chern insulator (a class A topological insulator) with introduced superconductivity. We study the phase diagram of the Chern insulator, then introduce superconductivity in the simplest possible form, continue on to build the topological phase diagram and characterize the system's strong and weak topological phases and edge modes, and finish by discussing the most general manner in which superconductivity can be introduced to the system.

4.1 A Simple Model for a 2D Chern Insulator

We begin with a simple model for a Chern Insulator, onto which we shall also introduce superconductivity in the next sections. The relative simplicity of the model, in conjunction with the fact that it will serve as a base for our more complicated model for which we will employ much of the same reasoning and methods, incentivises treating this model first.

We introduce a variation on the Bernevig-Hughes-Zhang (BHZ) model [34] for a 2D Chern Insulator:

$$\begin{gathered} H = \sum_{\boldsymbol{k}\in \mathrm{BZ}} \psi^{\dagger}\left(\boldsymbol{k}\right) H\left(\boldsymbol{k}\right) \psi\left(\boldsymbol{k}\right), \\ H\left(\boldsymbol{k}\right) = \left(m - t\left(\cos\left(k_x a\right) + \cos\left(k_y a\right)\right)\right)\sigma_z - \mu\mathbb{I} + A\sin\left(k_x a\right)\sigma_x + A\sin\left(k_y a\right)\sigma_y, \\ \text{and } \psi\left(\boldsymbol{k}\right) = \begin{pmatrix} a_{\boldsymbol{k}} \\ b_{\boldsymbol{k}} \end{pmatrix}. \end{gathered} \tag{32}$$

The above Hamiltonian is a momentum-space representation of a tight-binding model for electrons on a 2D square lattice, where our system is a spin-polarized system (suppressing the single spin specie's explicit notation) and the σ degree of freedom (σ are the Pauli matrices, $\mathbb{I}$ is the 2x2 identity matrix) signifies two orbitals a, b in each site, but could conceivably denote a two-atom unit cell or any other form of pseudo-spin. $a_{\boldsymbol{k}}, b_{\boldsymbol{k}}$ are the annihilation operators for electrons on a, b orbitals (respectively) with momentum $\boldsymbol{k}$.

In this case, a denotes the lattice constant (same in both x and y directions) - for brevity, we'll measure k_x, k_y in units of a^{-1} and therefore can set $a = 1$ in the Hamiltonian. m,t,μ and A are real variables as H is Hermitian.

To understand the physical meaning behind the Hamiltonian's parameters (32), we can also look at the

position-space representation of this Hamiltonian:

$$
\begin{aligned}
H &= H_{\text{on-site}} + \sum_{r=x,y} H^r_{\text{hopping}} + \sum_{r=x,y} H^r_{\text{cross-hopping}}, \\
H_{\text{on-site}} &= \sum_{\boldsymbol{r}} (m-\mu)\, a^\dagger_{\boldsymbol{r}} a_{\boldsymbol{r}} + (-m-\mu)\, b^\dagger_{\boldsymbol{r}} b_{\boldsymbol{r}}, \\
H^r_{\text{hopping}} &= \sum_{\boldsymbol{r}} -t\left(a^\dagger_{\boldsymbol{r}} a_{\boldsymbol{r}+\hat{r}} + a^\dagger_{\boldsymbol{r}+\hat{r}} a_{\boldsymbol{r}}\right) - t\left(b^\dagger_{\boldsymbol{r}} b_{\boldsymbol{r}+\hat{r}} + b^\dagger_{\boldsymbol{r}+\hat{r}} b_{\boldsymbol{r}}\right), \\
H^y_{\text{cross-hopping}} &= \sum_{\boldsymbol{r}} \frac{A}{2}\left(b^\dagger_{\boldsymbol{r}} a_{\boldsymbol{r}+\hat{y}} + a^\dagger_{\boldsymbol{r}+\hat{y}} b_{\boldsymbol{r}}\right) - \frac{A}{2}\left(a^\dagger_{\boldsymbol{r}} b_{\boldsymbol{r}+\hat{y}} + b^\dagger_{\boldsymbol{r}+\hat{y}} a_{\boldsymbol{r}}\right), \\
\text{and } H^x_{\text{cross-hopping}} &= \sum_{\boldsymbol{r}} \frac{A}{2i}\left(b^\dagger_{\boldsymbol{r}} a_{\boldsymbol{r}+\hat{x}} - a^\dagger_{\boldsymbol{r}+\hat{x}} b_{\boldsymbol{r}}\right) + \frac{A}{2i}\left(a^\dagger_{\boldsymbol{r}} b_{\boldsymbol{r}+\hat{x}} - b^\dagger_{\boldsymbol{r}+\hat{x}} a_{\boldsymbol{r}}\right).
\end{aligned}
\tag{33}
$$

Here $\boldsymbol{r}$ runs over the 2D square lattice with periodic boundary conditions and $\hat{r}$ is a unit vector in the $r = x, y$ direction. The on-site Hamiltonian contains a chemical potential term $-\mu$ (the energy both orbitals gain by electron occupation) and a "mass term" m (signifies the energy difference between the two orbitals, $2m$), t is the nearest-neighbor hopping coefficient for hopping between identical orbitals in both x and y directions and A is the nearest-neighbor hopping amplitude for hopping between different orbitals, where hopping in the x direction gains an i phase and hopping in the y direction gains no phase.

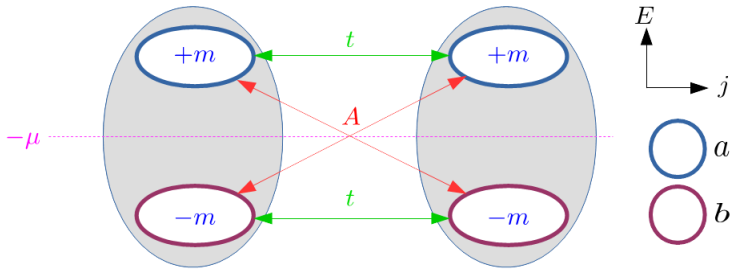

Figure 13: A schematic diagram of the relevant energy scales of the tight-binding Chern insulator Hamiltonian (32). The gray ellipse signifies a single site, where two electronic orbitals a, b with energies $-\mu \pm m$ reside. Electrons can tunnel to adjacent sites either to the same orbital (with amplitude t) or to the other orbital (with amplitude A). E is the energy axis and j is either x or y.

The momentum space Hamiltonian (32) can be displayed in the following form

$$
H(\boldsymbol{k}) = \boldsymbol{d}(\boldsymbol{k}) \cdot \boldsymbol{\sigma} - \mu \mathbb{I} \tag{34}
$$

$$
\boldsymbol{d}(\boldsymbol{k}) = \begin{pmatrix} A \sin k_x \\ A \sin k_y \\ m - t\cos k_x - t \cos k_y \end{pmatrix}, \quad \boldsymbol{\sigma} = \begin{pmatrix} \sigma_x \\ \sigma_y \\ \sigma_z \end{pmatrix}
$$

whose eigenvalues are always given as [1]:

$$
E_\pm = \pm |\boldsymbol{d}(\boldsymbol{k})| - \mu. \tag{35}
$$

We are interested in the topological phase diagram of this system - the relevant topological invariant is

the 1st Chern number which in the standard representation, using Berry curvature, is defined as [1]:

$$\nu = \sum_j \left[-\frac{i}{2\pi} \int_{BZ} d^2k \left(\langle \partial_{k_x} \psi_j(\boldsymbol{k}) | \partial_{k_y} \psi_j(\boldsymbol{k}) \rangle - \langle \partial_{k_y} \psi_j(\boldsymbol{k}) | \partial_{k_x} \psi_j(\boldsymbol{k}) \rangle \right) \right], \tag{36}$$

where j runs over all **filled** energy band indices, and $|\psi_j(\boldsymbol{k})\rangle$ are the corresponding eigenstates. The Chern number's value labels distinct topological phases for the system - however this does not necessarily mean that two phases with the same Chern number are in the same phase [17]. The Chern number is only well-defined for a gapped system - that is, a system where there is no contact point between bands at the Fermi energy (a contact point between a filled energy band and an unfilled energy band) [1].

As the Chern number is the system's topological invariant, it may only change its value after a closing and reopening of the energy gap under the change of some combination of the Hamiltonian's parameters. Therefore, it is enough to find the parameter values for which the gap closes to determine the curves in the parameter space which bound regions of parameter space where the Chern number can be different.

Choosing $\mu = 0$, we find that the gap between the energy bands closes only for $|\boldsymbol{d}(\boldsymbol{k})| = -|\boldsymbol{d}(\boldsymbol{k})| = 0$, or equivalently

$$\begin{pmatrix} A \sin k_x \\ A \sin k_y \\ m - t\cos k_x - t \cos k_y \end{pmatrix} = \boldsymbol{d}(\boldsymbol{k}) = 0. \tag{37}$$

Assuming $A \neq 0$ we find that the gap can close in exactly 4 unique points in the BZ, these closures requiring special values of $\frac{m}{t}$:

$$\begin{aligned} (k_x, k_y) = (0,0), \ \frac{m}{t} = 2, \\ (k_x, k_y) \in \{(0,\pi), (\pi, 0)\}, \ \frac{m}{t} = 0, \\ \text{and } \ (k_x, k_y) = (\pi, \pi), \ \frac{m}{t} = -2. \end{aligned} \tag{38}$$

Our topological phase diagram is therefore dependent only on the value of $\frac{m}{t}$. The gap closure points $\frac{m}{t} = 0, \pm 2$ set the phase boundaries, which translate to different values of the Chern number. From there on, it is enough to evaluate the Chern number for a single value of $\frac{m}{t}$ inside each possible phase to determine it for the entire phsae, and such an evaluation is easily done numerically. Both this method and a full numerical calculation of the Chern number for many $\frac{m}{t}$ points expectedly yield the same phase diagram, which can be seen in Figure (14).

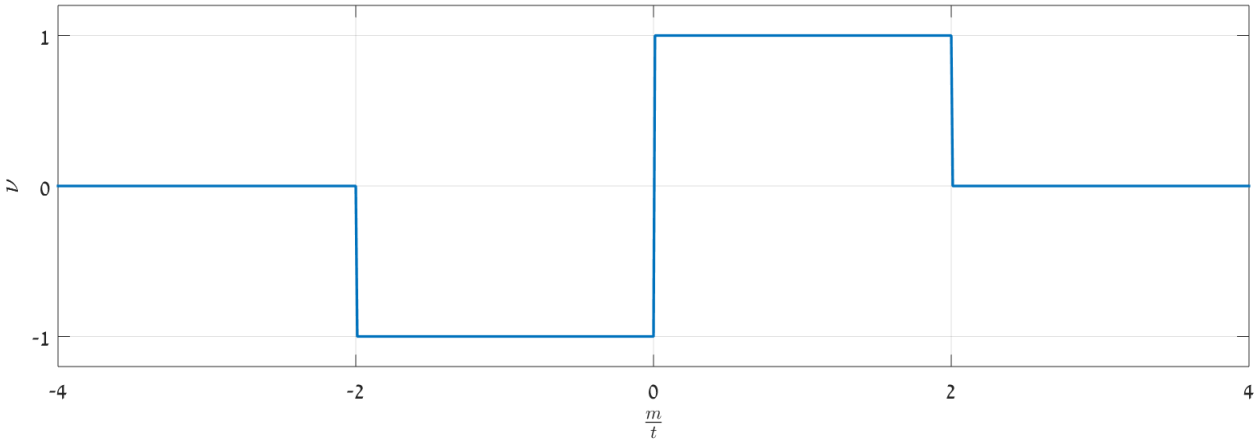

Figure 14: Phase diagram of our BHZ model for a Chern Insulator (32). There are 3 distinct topological phases: $\nu = 0$ ($\left|\frac{m}{t}\right| > 2$), $\nu = -1$ ($-2 < \frac{m}{t} < 0$) and $\nu = 1$ ($0 < \frac{m}{t} < 2$).

As we can see, this model already exhibits non-trivial topological characteristics (the Chern number for trivial systems is always $\nu = 0$).

We see that the parameter A has no effect on the topological phase diagram - we can explain this by noting that as long as $A \neq 0$, it does not determine the gap closure points or parameters.

The $\nu = 0$ sections ($\left|\frac{m}{t}\right| > 2$) can be intuitively understood by looking at the $\left|\frac{m}{t}\right| \to \infty$ limit, and noting there are no phase boundaries between that limit and $\frac{m}{t} = \pm 2$. In this limit m is much larger than the other energy scales t, A, equivalent to setting all hopping (t, A) to zero, as if each site was isolated from all other sites. This effectively creates two separated bands, each belonging only to a single orbital a, b (which band is higher and which band is lower is determined only by the sign of $\frac{m}{t}$), corresponding to a single electron per isolated site with a wavefunction completely localized, and therefore no topologically non-trivial phase can appear (such a phase is an inherently global entanglement phenomena [1]). This isolated atom picture is labeled the atomic limit.

The intermediate regime is also clear - starting from $\frac{m}{t} > 2$, we have $\nu = 0$. At $\frac{m}{t} = 2$, we have a gap closure at $(0, 0)$ and all other points (38) remain gapped, and for $0 < \frac{m}{t} < 2$ the Chern number is different. This suggests looking around the specific closure point for the cause, and so we can simplify and analyze the low-energy theory around it. The Chern number value we calculate in this approximated Hamiltonian can be anything (even non-integer) because the global band structure is different than the approximated one, but the difference between the Chern numbers for the approximated Hamiltonian before and after the closing and reopening of the band gap will be the correct change in the Chern number of the full Hamiltonian, as the change can only come from this local closure.

The Hamiltonian at that point is (equation (32)):

$$H(\boldsymbol{k}) = \begin{pmatrix} s & A(k_x - ik_y) \\ A(k_x + ik_y) & -s \end{pmatrix}, \tag{39}$$

where $s = m - 2t$. We notice that around $\frac{m}{t} \sim 2$, the s term changes sign. By direct calculation of the the low energy Hamiltonian Chern number it can be shown that

$$\nu = -\frac{\operatorname{sgn}(s)}{2} \tag{40}$$

And therefore the Chern number increases by $\delta\nu = 1$ when going from $\frac{m}{t} > 2$ to $0 < \frac{m}{t} < 2$. As $\nu = 0$ for $\frac{m}{t} > 2$, we have $\nu = 1$ for $0 < \frac{m}{t} < 2$.

The observation (40) can actually be generalized for any low energy theory which gives a Dirac-cone dispersion at the gap closure points $s = 0$, of a form similar to (39):

$$H(\boldsymbol{k}) = \eta k_x \sigma_x + \xi k_y \sigma_y + s\sigma_z \ , \ \eta, \xi \in \{\pm 1\}, \tag{41}$$

$$\nu = -\frac{1}{2}\mathrm{sgn}(\eta\xi)\,\mathrm{sgn}(s), \tag{42}$$

$$\delta\nu = \mathrm{sgn}(\eta\xi), \tag{43}$$

where $\delta\nu$ is calculated across a phase boundary line where s changes sign from positive ($\mathrm{sgn}(s) > 0$) to negative ($\mathrm{sgn}(s) < 0$)

The general observation is that such a closing and reopening of a Dirac cone gap changes the Chern number by ± 1. A similar procedure can be performed for the gap closure points relevant to rest of the parameter range, yielding the complete phase diagram.

It should be noted that our result is expected within the existing classification of topological phases. Our Chern insulator Hamiltonian (32) describes a 2D system and possesses neither time-reversal symmetry, nor particle-hole symmetry nor chiral symmetry [34], and therefore belongs to the topological class A with a $\mathbb{Z}$ topological invariant. This is the Chern number, which we have indeed found to take the values $0, \pm 1$.

4.2 Introducing p-wave Superconductivity

We wish to induce a superconducting pairing (Cooper channel) onto our Chern insulator system. This pairing cannot be of the common s-wave pairing form which couples electrons of opposite spins (encourages Cooper pairs formed of electrons with opposite spin) as our system is spin-polarized (has only electrons from a single spin specie - either $\uparrow$ or $\downarrow$), and so should be of p-wave superconductivity form (coupling electrons of the same spin)[1]. The most general such term we can add, framing it in the standard mean-field fashion as a non particle-number conserving term, is of the form (in momentum space):

$$H_{\mathrm{SC}} = 2\sum_{\boldsymbol{k}} \Delta_{aa}(\boldsymbol{k})\, a_{-\boldsymbol{k}} a_{\boldsymbol{k}} + \Delta_{bb}(\boldsymbol{k})\, b_{-\boldsymbol{k}} b_{\boldsymbol{k}} + \tilde{\Delta}_{ab}(\boldsymbol{k})\, a_{-\boldsymbol{k}} b_{\boldsymbol{k}} + \tilde{\Delta}_{ba}(\boldsymbol{k})\, b_{-\boldsymbol{k}} a_{\boldsymbol{k}} + h.c. \ . \tag{44}$$

We stress that only couplings between electrons pairs with momenta $\boldsymbol{k}$ and $-\boldsymbol{k}$ is allowed, rather than any momenta pair $\boldsymbol{k}$ and $\boldsymbol{k'}$. The origin of this restriction is our mean-field treatment of the Cooper channel (where it is assumed that the significant electron pairing channel is with total momentum zero). Using the anti-commutation relation of the fermion operators $\{b_{\boldsymbol{k}}, b_{\boldsymbol{q}}\} = \{a_{\boldsymbol{k}}, a_{\boldsymbol{q}}\} = \{a_{\boldsymbol{k}}, b_{\boldsymbol{q}}\} = 0$ and the fact that summation over BZ momenta is symmetric w.r.t. to inversion $\boldsymbol{k} \to -\boldsymbol{k}$, we notice that the diagonal terms must be antisymmetric:

$$\Delta_{aa}(\boldsymbol{k}) = -\Delta_{aa}(-\boldsymbol{k}), \tag{45}$$
$$\Delta_{bb}(\boldsymbol{k}) = -\Delta_{bb}(-\boldsymbol{k}),$$

and also that the last two terms can be redefined as:

$$\Delta_{ba}(\boldsymbol{k})\, b_{-\boldsymbol{k}} a_{\boldsymbol{k}} - \Delta_{ba}(-\boldsymbol{k})\, a_{-\boldsymbol{k}} b_{\boldsymbol{k}}. \tag{46}$$

In matrix form it is written as

$$H_{\mathrm{SC}} = \sum_{\boldsymbol{k}} \begin{pmatrix} a_{-\boldsymbol{k}} & b_{-\boldsymbol{k}} \end{pmatrix} \Delta(\boldsymbol{k}) \begin{pmatrix} a_{\boldsymbol{k}} \\ b_{\boldsymbol{k}} \end{pmatrix},$$
$$\Delta(\boldsymbol{k}) = \begin{pmatrix} \Delta_{aa}(\boldsymbol{k}) & \Delta_{ba}(\boldsymbol{k}) \\ -\Delta_{ba}(-\boldsymbol{k}) & \Delta_{bb}(\boldsymbol{k}) \end{pmatrix}. \tag{47}$$

Moreover, we require consistency with our nearest-neighbor tight-binding Hamiltonian which restricts the possible superconducting pairing terms in real space up to nearest-neighbor terms. In momentum space, this translates to momentum dependency of the matrix elements that is either constant or that depends solely on $\boldsymbol{k}\cdot\boldsymbol{a}$ as an argument of 2π-periodic trigonometric terms (cos,sin), with $\boldsymbol{a}$ being any primitive lattice vectors ($a\hat{x}, a\hat{y}$ in our case).

As our original Chern insulator Hamiltonian (32) has no time-reversal symmetry, particle-hole symmetry or chiral symmetry, there are no further limitation to our possible pairing terms. Aggregating the above conclusions and equations (45),(47) and assuming that the pairing is isotropic in amplitude, we find that

$$\begin{aligned} \Delta_{aa}(\boldsymbol{k}) &= \Delta^{s}_{aa}\left(\sin k_x + e^{i\varphi}\sin k_y\right), \\ \Delta_{bb}(\boldsymbol{k}) &= \Delta^{s}_{bb}\left(\sin k_x + e^{i\varphi}\sin k_y\right), \\ \text{and } \Delta_{ba}(\boldsymbol{k}) &= \Delta^{0}_{ba} + \Delta^{s}_{ba}\left(\sin k_x + e^{i\phi}\sin k_y\right) + \Delta^{c}_{ba}\left(\cos k_x + e^{i\varphi}\cos k_y\right) \end{aligned} \tag{48}$$

are the most general terms we can write for our model.

To start, we choose the simplest possible pairing - only taking the constant (on-site) term Δ^{0}_{ab} to be nonzero, while setting all other terms to zero. This can be interpreted as an approximation treating intra-site superconductivity as negligible but inter-site superconductivity as significant in our system, meaning superconductivity is strongly suppressed in distance for all types of superconducting pairing:

$$\Delta^{0}_{ba} \gg \Delta^{s}_{aa}, \Delta^{s}_{bb}, \Delta^{s}_{ba}, \Delta^{c}_{ba}. \tag{49}$$

Relabeling $\Delta^{0}_{ba} \equiv \Delta$, this gives our SC term as

$$H_{SC} = \sum_{\boldsymbol{k}} \begin{pmatrix} a_{\boldsymbol{k}} & b_{\boldsymbol{k}} \end{pmatrix} \Delta(\boldsymbol{k}) \begin{pmatrix} a_{-\boldsymbol{k}} \\ b_{-\boldsymbol{k}} \end{pmatrix} + h.c., \tag{50}$$
$$\text{and } \Delta(\boldsymbol{k}) = \begin{pmatrix} 0 & \Delta \\ -\Delta & 0 \end{pmatrix}.$$

Here we can assume Δ to be real , as it can be made so by redefining the annihilation operators with an additional phase [35].

4.3 Chern Number Characterization of the Model

Next, by casting our existing Hamiltonian H and superconducting pairing H_{SC} into the standard Bogoliubov-de Gennes (BdG) Hamiltonian form, with the following standard definitions the BdG Hamiltonian $H_{\mathrm{BdG}}(\boldsymbol{k})$

and Nambu spinor $\Psi_{\boldsymbol{k}}$ [35]:

$$H = \frac{1}{2}\sum_{\boldsymbol{k}\in \mathrm{BZ}} \left(\Psi_{\boldsymbol{k}}^{\dagger} H_{\mathrm{BdG}} \Psi_{\boldsymbol{k}} + \mathrm{Tr}\left(H\left(\boldsymbol{k}\right)\right)\right), \tag{51}$$

$$H_{\mathrm{BdG}}\left(\boldsymbol{k}\right) = \begin{pmatrix} H\left(\boldsymbol{k}\right) & \Delta\left(\boldsymbol{k}\right) \\ \Delta^{\dagger}\left(\boldsymbol{k}\right) & -H^{T}\left(-\boldsymbol{k}\right) \end{pmatrix}, \tag{52}$$

$$\text{and } \Psi_{\boldsymbol{k}}^{\dagger} = \begin{pmatrix} a_{\boldsymbol{k}}^{\dagger} & b_{\boldsymbol{k}}^{\dagger} & a_{-\boldsymbol{k}} & b_{-\boldsymbol{k}} \end{pmatrix}, \ \Psi_{\boldsymbol{k}} = \begin{pmatrix} a_{\boldsymbol{k}} \\ b_{\boldsymbol{k}} \\ a_{-\boldsymbol{k}}^{\dagger} \\ b_{-\boldsymbol{k}}^{\dagger} \end{pmatrix}, \tag{53}$$

with T for transpose. We have:

$$H\left(\boldsymbol{k}\right) = \begin{pmatrix} \left(m - t\cos k_x - t\cos k_y\right) - \mu & A\left(\sin k_x - i\sin k_y\right) \\ A\left(\sin k_x + i\sin k_y\right) & -\left(m - t\cos k_x - t\cos k_y\right) - \mu \end{pmatrix}, \tag{54}$$

$$\text{and } H^{T}\left(-\boldsymbol{k}\right) = \begin{pmatrix} -\left(m - t\cos k_x - t\cos k_y\right) + \mu & A\left(\sin k_x + i\sin k_y\right) \\ A\left(\sin k_x - i\sin k_y\right) & \left(m - t\cos k_x - t\cos k_y\right) + \mu \end{pmatrix}. \tag{55}$$

With τ representing Pauli matrices in the particle-hole subspace and σ representing Pauli matrices in the orbital subspace (as before), we can write our BdG Hamiltonian in more compact form as:

$$H_{\mathrm{BdG}}\left(\boldsymbol{k}\right) = A\sin k_x \sigma_x + A\sin k_y \sigma_y \tau_z + \left(m - t\cos k_x - t\cos k_y\right)\sigma_z \tau_z - \Delta \sigma_y \tau_y - \mu \tau_z. \tag{56}$$

Next, disregarding the constant contribution $\frac{1}{2}\sum_{\boldsymbol{k}\in \mathrm{BZ}} \mathrm{Tr}\left(H\left(\boldsymbol{k}\right)\right)$, we find the energy bands. By noticing σ and τ work in orthogonal subspaces, using the properties of Pauli matrix products and squaring the Hamiltonian equation twice, it is straightforward to show that the energy bands are $\pm E_{\pm}\left(\boldsymbol{k}\right)$, where:

$$E_{\pm}\left(\boldsymbol{k}\right) = \sqrt{\left(A^2(\sin^2 k_x + \sin^2 k_y) + (m - t\cos k_x - t\cos k_y)^2 + \Delta^2 + \mu^2\right) \pm 2\sqrt{\mu^2 A^2(\sin^2 k_x + \sin^2 k_y) + (m - t\cos k_x - t\cos k_y)^2(\Delta^2 + \mu^2)}}. \tag{57}$$

According to (57), the energy bands satisfy

$$-E_{+}\left(\boldsymbol{k}\right) \leq -E_{-}\left(\boldsymbol{k}\right) \leq 0 \leq E_{-}\left(\boldsymbol{k}\right) \leq E_{+}\left(\boldsymbol{k}\right), \tag{58}$$

meaning the ground state of the system is where the two bands with negative energy, $-E_{\pm}\left(\boldsymbol{k}\right)$, are filled. Moreover, to get a band crossing between filled and empty bands we must have $E_{-}\left(\boldsymbol{k}\right) = 0$, as imposed by inequality (58). To obtain the topological phase diagram we must determine for what parameter range (and at which $\boldsymbol{k}$) this crossing can occur. As explained in the previous part, the parameters ranges corresponding to possible gap closure points are the only curves in the phase diagram which can delineate different phases. This is translated to the requirement $E_{-}\left(\boldsymbol{k}\right) = 0$, which can be simplified after some nontrivial manipulation to:

$$\left(A^2\left(\sin^2 k_x + \sin^2 k_y\right) + \left(m - t\cos k_x - t\cos k_y\right)^2 - \left(\Delta^2 + \mu^2\right)\right)^2 + 4A^2\Delta^2\left(\sin^2 k_x + \sin^2 k_y\right) = 0. \tag{59}$$

We note that the two terms are non-negative, meaning they must both be zero for this equality to hold,

translating to the requirements:

$$A^2\left(\sin^2 k_x+\sin^2 k_y\right)+\left(m-t\cos k_x-t\cos k_y\right)^2-\left(\Delta^2+\mu^2\right)=0, \tag{60}$$

$$4A^2\Delta^2\left(\sin^2 k_x+\sin^2 k_y\right)=0. \tag{61}$$

We assume as before $A\neq 0$ and also nontrivial superconductivity $\Delta\neq 0$ (the $\Delta=0$ case was solved in the previous section), turning the second requirement (61) (as a sum of non-negative terms) to

$$\sin k_x=\sin k_y=0. \tag{62}$$

Meaning this band gap closure can only occur at the 4 high symmetry points of the 2D BZ (which we denote as $\mathbf{\Gamma}_i$):

$$(k_x,k_y)\in\{\mathbf{\Gamma}_i\}_{i=1}^4=\{(0,0),(0,\pi),(\pi,0),(\pi,\pi)\} \tag{63}$$

which are the exact same gap closure points we found in the previous case with no SC (equation (38)). The high symmetry points are so called because they are the only points in the BZ which satisfy $-\mathbf{\Gamma}_i=\mathbf{\Gamma}_i+\boldsymbol{G}$ for all reciprocal lattice vectors $\boldsymbol{G}\in\left\{\left(\frac{2\pi}{a},0\right),\left(0,\frac{2\pi}{a}\right)\right\}$., which will be useful later.

Denoting as before:

$$d_z\left(k_x,k_y\right)\equiv m-t\cos k_x-t\cos k_y, \tag{64}$$

we find that at these points

$$\begin{aligned} d_z\left(0,0\right)&\equiv m-2t,\\ d_z\left(0,\pi\right)=d_z\left(\pi,0\right)&\equiv m,\\ \text{and } d_z\left(\pi,\pi\right)&\equiv m+2t. \end{aligned} \tag{65}$$

The first requirement (60), which is relevant for only these special points now, gives

$$d_z\left(k_x,k_y\right)=\pm\sqrt{\Delta^2+\mu^2}, \tag{66}$$

so the appropriate gap-closure parameter curves, with the corresponding points in the BZ where the gap closes, are:

$$\begin{aligned} (0,0):\ m&=\pm\sqrt{\Delta^2+\mu^2}+2t,\\ (0,\pi),(\pi,0):\ m&=\pm\sqrt{\Delta^2+\mu^2},\\ \text{and }\ (\pi,\pi):\ m&=\pm\sqrt{\Delta^2+\mu^2}-2t. \end{aligned} \tag{67}$$

At the $\Delta,\mu\to 0$ limit we indeed recover the result from the previous section $\frac{m}{t}=\pm 2,0$ at the appropriate points in the BZ. Equation (67) shows the phase diagram is symmetric w.r.t. $\Delta,-\Delta$ and $\mu,-\mu$ (as only Δ^2,μ^2 appear in the phase boundary expression) and depends only on $\sqrt{\Delta^2+\mu^2}$ (not on Δ or μ separately).

Dividing by t, we therefore have only two parameters which determine the phase diagram, $\frac{m}{t}$ and $\frac{\sqrt{\Delta^2+\mu^2}}{t}$. The appearance of Δ and μ on the same footing as a single, equally weighted parameter $\sqrt{\Delta^2+\mu^2}$ which determines the phase space structure signifies the fact that they are complementary energy scales for inter-site electron occupation - introducing an electron to an orbital gains $-\mu$ energy, and the intra-site Cooper channel strives to fill sites with either two electrons or zero electrons with an energy benefit from the SC

pairing Δ. This is contrasted with the $\frac{m}{t}$ term, which aspires to make only a single orbital beneficial for occupation, as it determines the energy difference between the two.

The same analytical method as was used in the previous section can again be utilized to find the phase diagram. It utilizes the low energy theory around the gapless points when the parameter values approach their critical values (equation (67)) to determine changes in the Chern number. We start from a familiar regime in the phase diagram - $\Delta = \mu = 0$, $\frac{m}{t} > 2$ which we analyzed in the previous section and corresponds to a topologically trivial phase $\nu = 0$. From there on we can calculate the Chern number change each time we cross a phase boundary line, until we have them all. The result of this analytical calculation, with phase boundaries and the values of the Chern number verified numerically, can be seen in Figure (15).

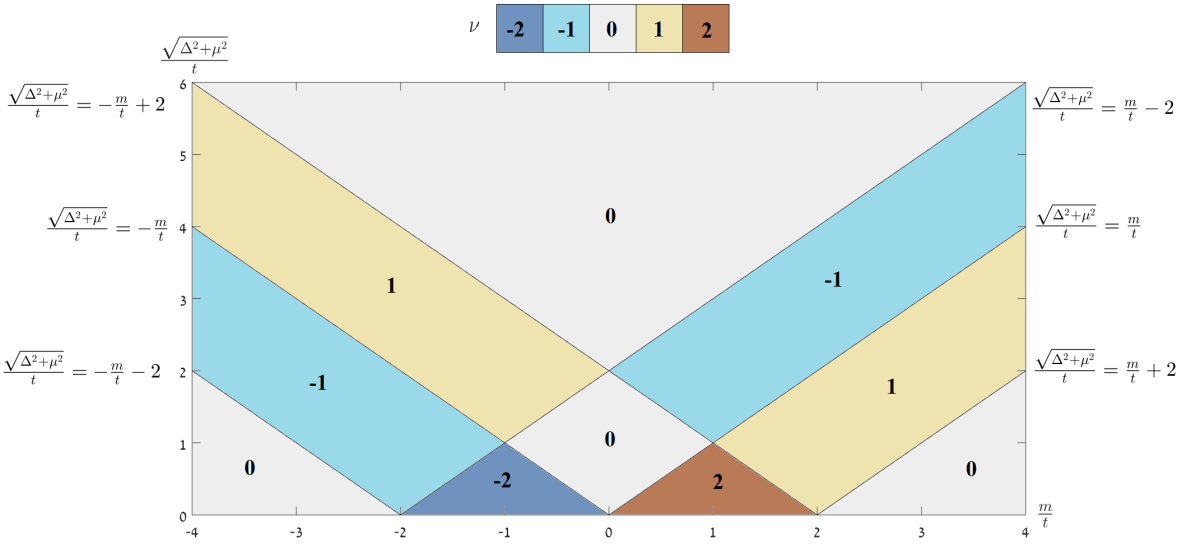

Figure 15: Phase diagram of the model in equation (56), plotted in the $\frac{\sqrt{\Delta^2+\mu^2}}{t}$ vs. $\frac{m}{t}$ plane. Different colors represent different Chern numbers, calculated numerically, with a color key brought at the top. Phase boundary lines are labeled at the sides.

The Chern numbers at the $\mu = \Delta = 0$ cut of the diagram seem doubled w.r.t. to our Chern number calculated in the previous section. This is because the Chern number we calculate now is effectively twice the previous one, doubled by the artificial doubling of degrees of freedom which was used to construct the BdG Hamiltonian (56) (in this BdG formalism there are now two filled bands instead of one in this limit, each contributing to the Chern number). We shall deal with the significance of these values of the Chern number in determining the edge mode properties of the system in the next section.

Looking at the phase diagram, we notice that some disjointed parts of the phase diagram possess the same Chern number, which leads us to suspect these could represent different phases (albeit with the same Chern number). This, coupled with our desire to understand the edge modes corresponding to these phases when translational symmetry in some direction is removed, motivates us to look for additional indices to characterize our system, which will lead us to introduce the concept of weak topological phases.

4.4 Weak Topological Phases and the Full Topological Phase Diagram

We can find 2 more indices which characterize our system. This can be done as long as the only gap closure points of the Hamiltonian are the high symmetry points $\mathbf{\Gamma}_i$ [18, 21], which is indeed true in our case (see equations (62),(63)). We do this by analyzing the properties of our Hamiltonian at the high symmetry points $\mathbf{\Gamma}_i$ at any well-defined topological phase (gapped phase).

To derive these new indices, we will use the fact that our BdG Hamiltonian has particle-hole symmetry (an anti-unitary operator which anti-commutes with the Hamiltonian):

$$CH_{\mathrm{BdG}}\left(\boldsymbol{k}\right)C^{-1}=-H_{\mathrm{BdG}}\left(\boldsymbol{k}\right), \tag{68}$$

with the symmetry operator being

$$C\equiv\tau_x K, \tag{69}$$

where K is the complex conjugation operator (is also anti-unitary [takes $\boldsymbol{k}\to-\boldsymbol{k}$] with $K^2=1$), as can be checked explicitly using the explicit expression for $H_{\mathrm{BdG}}\left(\boldsymbol{k}\right)$ in terms of σ,τ matrices.

It should be noted that we still have no Time-Reversal symmetry and therefore no Chiral symmetry as well, so this along with $C^2=1$ classifies our system as topological class D, and as our system is 2D this means it should have a $\mathbb{Z}$ topological invariant, which is again the Chern number.

Using the fact that $H_{\mathrm{BdG}}^{\dagger}\left(\boldsymbol{k}\right)=H_{\mathrm{BdG}}\left(\boldsymbol{k}\right)$ and the properties of the conjugation operator, equation (68) can be restated as $\tau_x H_{\mathrm{BdG}}\left(\boldsymbol{k}\right)\tau_x=-H_{\mathrm{BdG}}^{T}\left(-\boldsymbol{k}\right)$, which at the high symmetry points turns into (using the properties of these points and the BZ property $H_{\mathrm{BdG}}\left(\boldsymbol{k}+\boldsymbol{G}\right)=H_{\mathrm{BdG}}\left(\boldsymbol{k}\right)$):

$$\tau_x H_{\mathrm{BdG}}\left(\mathbf{\Gamma}_i\right)\tau_x=-H_{\mathrm{BdG}}^{T}\left(\mathbf{\Gamma}_i\right). \tag{70}$$

Using this property we can show that an equivalent Hamiltonian $\tilde{H_{\mathrm{BdG}}}\left(\mathbf{\Gamma}_i\right)=UH_{\mathrm{BdG}}\left(\mathbf{\Gamma}_i\right)U^{-1}$ gained by a change of basis using the unitary transformation $U=e^{i\frac{\pi}{4}\tau_x}$ gives an anti-symmetric form $\tilde{H_{\mathrm{BdG}}}^{T}\left(\mathbf{\Gamma}_i\right)=-\tilde{H_{\mathrm{BdG}}}\left(\mathbf{\Gamma}_i\right)$, which makes the Pffafian of this matrix well defined. We can use the property $\det\left(\tilde{H_{\mathrm{BdG}}}\left(\mathbf{\Gamma}_i\right)\right)=\left(\mathrm{pf}\left(\tilde{H_{\mathrm{BdG}}}\left(\mathbf{\Gamma}_i\right)\right)\right)^2$ and the invariance of the determinant under unitary transformation to find

$$\left(\mathrm{pf}\left(\tilde{H_{\mathrm{BdG}}}\left(\mathbf{\Gamma}_i\right)\right)\right)^2=\det\left(H_{\mathrm{BdG}}\left(\mathbf{\Gamma}_i\right)\right). \tag{71}$$

Direct calculation of the determinant at the high symmetry points is easy because $H_{\mathrm{BdG}}\left(\mathbf{\Gamma}_i\right)$ is in block diagonal form (see equation (56)). We get two possible values

$$\mathrm{pf}\left(\tilde{H_{\mathrm{BdG}}}\left(\mathbf{\Gamma}_i\right)\right)=\pm\left(\mu^2+\Delta^2-d_z\left(\mathbf{\Gamma}_i\right)^2\right). \tag{72}$$

This sets the Pffafian up to a sign, which will not matter as the relevant topological indices will be dependent only on the signs of products of such Pffafians (and so an overall minus sign to the definition will leave the indices invariant) [21]. We choose:

$$\mathrm{pf}\left(\tilde{H_{BdG}}\left(\mathbf{\Gamma}_i\right)\right)=\mu^2+\Delta^2-d_z\left(\mathbf{\Gamma}_i\right)^2. \tag{73}$$

Next, we define

$$s_{\mathbf{\Gamma}_i}\equiv\mathrm{sgn}\left(-\mathrm{pf}\left(\tilde{H_{BdG}}\left(\mathbf{\Gamma}_i\right)\right)\right) \tag{74}$$

And four topological indices $\nu_{x,0}, \nu_{x,\pi}, \nu_{y,0}, \nu_{x,\pi}$ (defined modulo 2) via [15, 21]:

$$\begin{aligned}(-1)^{\nu_{x,0}} &= s_{(0,0)}s_{(0,\pi)},\\ (-1)^{\nu_{x,\pi}} &= s_{(\pi,0)}s_{(\pi,\pi)},\\ (-1)^{\nu_{y,0}} &= s_{(0,0)}s_{(\pi,0)},\\ (-1)^{\nu_{y,\pi}} &= s_{(0,\pi)}s_{(\pi,\pi)},\end{aligned} \tag{75}$$

where $\nu_{i,p}$ $(i = x, y,\ p = 0, \pi)$ are topological invariants of effective 1D systems which belong to the topological class D, with a fixed momenta coordinate in the i direction $k_i = p$ [5, 18]. The high symmetry points in the BZ, the $s_{\mathbf{\Gamma}_i}$ variables defined at these points and their relations to the indices are illustrated in Figure (16).

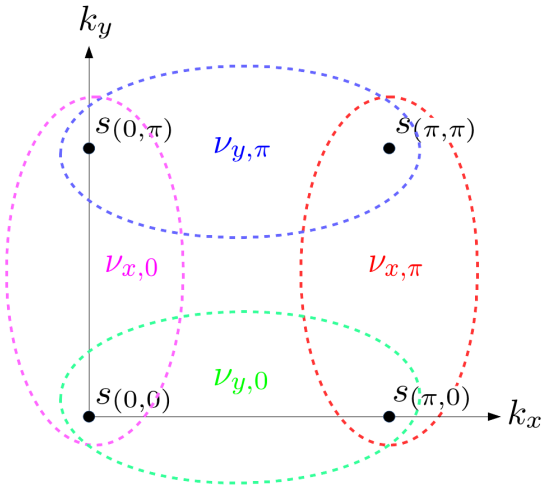

Figure 16: Definition of the weak indices $\nu_{x,0}, \nu_{x,\pi}, \nu_{y,0}, \nu_{y,\pi}$ via products of pairs of $s_{\mathbf{\Gamma}_i}$-s, defined in the BZ (equation (75)). $s_{\mathbf{\Gamma}_i}$ are in turn determined by the Pfaffians of the Hamiltonian at the 4 high symmetry points $\mathbf{\Gamma}_i$ (equation (74)). All topological phases can be characterized 2 weak indices (one in each direction) and a strong index, ν (equation (76)). The two weak indices chosen here are $\nu_{x,\pi}$ and $\nu_{y,\pi}$ (highlighted by the red and blue dashed ellipses).

Equations (73),(74) imply that the weak indices can change their value only at the previously determined phase boundaries (67), which we found using our previous method relating to the Chern number. This is part of a more general truth, with the weak indices being related to the Chern number by [18, 21]:

$$\nu_{x,0} + \nu_{x,\pi} = \nu_{y,0} + \nu_{y,\pi} = \nu \mod 2, \tag{76}$$

which establishes codependency between the indices, such that to determine the topological phase of the system one can use only a single index with an x label, a single index with a y label and the Chern number. We choose $\nu_{x,\pi}, \nu_{y,\pi} \in \mathbb{Z}_2$ as well as the mandatory $\nu \in \mathbb{Z}$, and denote the phase as

$$\nu : \nu_{x,\pi}\nu_{y,\pi} \tag{77}$$

Using equations (73), (74), (75) we can easily compute $\nu_{x,\pi}, \nu_{y,\pi}$ and further label the phase diagram, as can be seen in Figure (17).

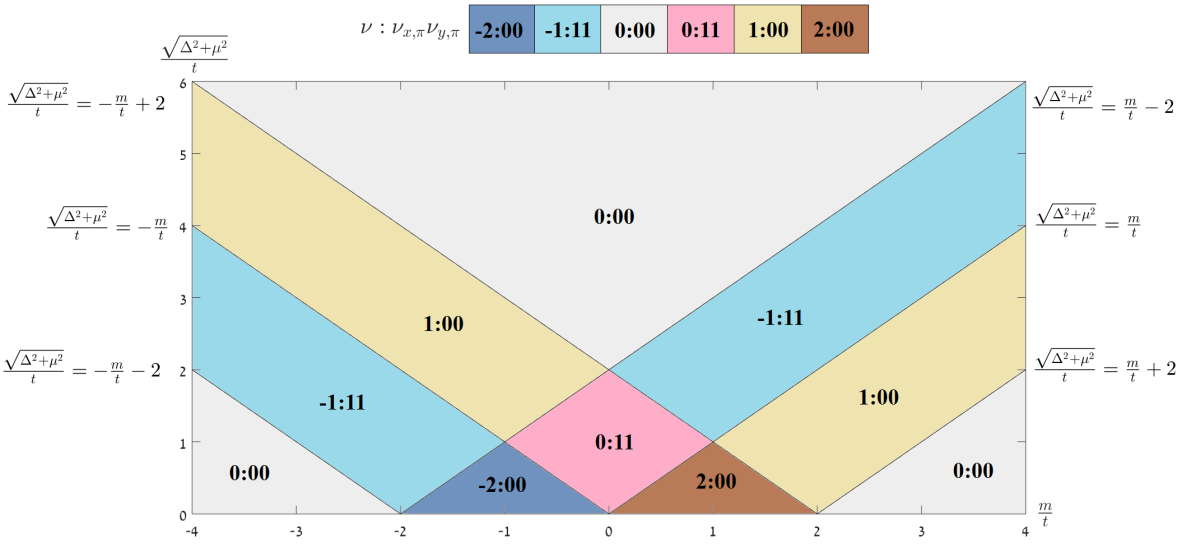

Figure 17: Full topological phase diagram of the model in equation (56), including both strong and weak topological indices calculated analytically and verified numerically, labeled in the $\nu : \nu_{x,\pi}\nu_{y,\pi}$ convention (equation (77)) and plotted in the $\frac{\sqrt{\Delta^2+\mu^2}}{t}$ vs. $\frac{m}{t}$ plane. Different colors represent different phases, with a color key brought at the top. Phase boundary lines are labeled to the sides.

Looking at Figure (17), we are convinced the trio $\nu : \nu_{x,\pi}\nu_{y,\pi}$ uniquely labels our phases, which now leads us to interpret the physical significance these three indices have.

It is an established observation that the Chern number ν of the system gives the total number of chiral edge modes (electron and\or hole excitations which travel along the edge of the system), where the sign for each term in the sum is determined by a the chirality of the corresponding edge mode (1 or -1). Furthermore, the presence of these chiral edge modes does not rely on any symmetry, and is robust (in the sense that they remain in the face of weak perturbations) [1]. This motivates the labeling of phases with a nonzero Chern number as strong topological phases, and the Chern number itself as a strong topological index.

In addition, in the presence of translational symmetry in the x, y directions we can always define two $\mathbb{Z}_2$ indices which count the parity of the number of edge modes in each such direction respectively - these are in fact the two other indices $\nu_{x,\pi}, \nu_{y,\pi}$ respectively [15, 21].

Also note that an $\nu_{i,p}$ index as we defined it is only well defined as long as there is translational invariance in the i direction - it is in this sense, the lack of robustness of the resulting edge modes, that these indices are labeled weak topological indices. A phase with $\nu = 0$ but nonzero weak indices is therefore labeled a weak topological phase.

The practical meaning of this is that, for example, in the presence of a boundary exactly parallel to the x axis a copy of our system in the weak topological phase $0 : 11$ and a copy of our system in the trivial phase $0 : 00$, there will be two counter-propagating Majorana zero energy edge modes with $k_x = 0$ and $k_x = \pi$, as we actually show by explicit construction in Appendix (7.3). A summary of the phases appearing in our system and their corresponding edge mode configurations is given in Table (1):

	$\nu : \nu_{x,\pi}\nu_{y,\pi}$	$s_{(0,\pi)}$ $s_{(\pi,\pi)}$ $s_{(0,0)}$ $s_{(\pi,0)}$	**Edge States (Chiral Majorana modes)**
Trivial Phase	0:00	$+ \; + \; , \; - \; -$ $+ \; + \; , \; - \; -$	None
Weak Phase	0:11	$- \; +$ $+ \; -$	Non-chiral modes along edges parallel to x and y
Strong Phases	-1:11	$+ \; - \; , \; - \; +$ $+ \; + \; , \; - \; -$	Single $\mathcal{C} = -1$ mode along edges parallel to x with $k_x = \pi$ and parallel to y with $k_y = \pi$
	1:00	$+ \; + \; , \; - \; -$ $- \; + \; , \; + \; -$	Single $\mathcal{C} = +1$ mode along edges parallel to x with $k_x = 0$ and parallel to y with $k_y = 0$
	-2:00	$+ \; +$ $+ \; +$	Two $\mathcal{C} = -1$ modes along edges parallel to x and y with either both at $k_x = 0, k_y = 0$ or both at $k_x = \pi, k_y = \pi$
	2:00	$+ \; +$ $+ \; +$	Two $\mathcal{C} = +1$ modes along edges parallel to x and y with either both at $k_x = 0, k_y = 0$ or both at $k_x = \pi, k_y = \pi$

Table 1: All possible topological phases and their edge states. Chirality is denoted by $\mathcal{C}$. The first column describes the nature of each topological phase (trivial, weak or strong), the second labels it in the $\nu : \nu_{x,\pi}\nu_{y,\pi}$ convention (equation (77)), the third details the corresponding $s_{\mathbf{\Gamma}_i}$ configurations where ± 1 is labeled $\pm$ (equations (74)) and the fourth details the deduced edge mode configurations.

It should be noted that the "two Majorana chiral edge mode" phases $2:00, -2:00$ should agree with the Chern insulator topological phase at $\Delta = \mu = 0$. The reconciliation comes from the fact that the ± 1 BHZ Chern insulator phases house a single ± 1 chirality electronic edge mode [34] and an electronic edge mode can always be decomposed into two co-propagating Majorana edge modes, and the fact that the SC Chern number ν counts the chirality-weighed total number of Majorana edge modes, while the Chern insulator Chern number counts the number of electronic edge modes.

Therefore, our system's phases with an even Chern number have either electronic edge modes ($\nu = \pm 2$) or no edge modes ($\nu = 0$), and those with an odd Chern number have Majorana edge modes ($\nu = \pm 1$).

Also, the sought-after topological phase with a single Majorana chiral edge mode suggested for quantum computation is realizable in our system as the phases $-1:11, 1:00$.

4.5 Generalizing to Weak Superconducting Pairing

We can now treat the superconducting pairing in its full generality, returning to the most general permissible form in equation (48), with now all non-Δ^0_{ab} pairings nonzero but weak. The pairings are to be weak in the sense that they do not create possible gapless points in the BZ outside of the 4 high symmetry points $\mathbf{\Gamma}_i$. In such a case our weak indices are still well defined, and we can retrace the steps of our analysis. The phase boundaries are still determined by the Pffafian defined by equation (71) at the high symmetry points. Then it is enough to look only at $\Delta(\mathbf{\Gamma}_i)$:

$$\Delta(\mathbf{\Gamma}_i) = \begin{pmatrix} 0 & \tilde{\Delta}(\mathbf{\Gamma}_i) \\ -\tilde{\Delta}(\mathbf{\Gamma}_i) & 0 \end{pmatrix},$$
$$\tilde{\Delta}(\mathbf{\Gamma}_i) \equiv \Delta^0_{ba} + \Delta^c_{ba}\left(\cos\Gamma^x_i + \cos\Gamma^y_i\right), \tag{78}$$

$$\begin{aligned}\tilde{\Delta}(0,0) &= \Delta^0_{ba} + 2\Delta^c_{ba}, \\ \tilde{\Delta}(0,\pi) = \tilde{\Delta}(0,\pi) &= \Delta^0_{ba}, \\ \tilde{\Delta}(\pi,0) &= \Delta^0_{ba} - 2\Delta^c_{ba},\end{aligned} \tag{79}$$

This is the same form of the $\Delta(\boldsymbol{k})$ matrix we had previously in equation (50) at the high symmetry points, with $\tilde{\Delta}(\boldsymbol{\Gamma}_i)$ instead of Δ (now a complex variable instead of a real one, but the solutions will still depend on $\left|\tilde{\Delta}\right|$ as they did before), now depending on the point of choice $\boldsymbol{\Gamma}_i$ and generally $\tilde{\Delta}(\boldsymbol{\Gamma}_i) \neq \tilde{\Delta}(\boldsymbol{\Gamma}_j)$. Therefore, the weak indices are now defined via

$$s_{\boldsymbol{\Gamma}_i} = \text{sign}\left(d_z(\boldsymbol{\Gamma}_i)^2 - \left(\mu^2 + |\Delta(\boldsymbol{\Gamma}_i)|^2\right)\right) \tag{80}$$

and the phase boundaries are set by the solution to the 4 equations

$$d_z(\boldsymbol{\Gamma}_i)^2 = \mu^2 + |\Delta(\boldsymbol{\Gamma}_i)|^2 \tag{81}$$

as before. We can therefore expect a similar phase diagram which is easily interpolated from the phase diagram in Figure (17) ($\Delta^c_{ba} = 0$), albeit with slightly modified phase boundaries.

A specific example to the general analysis above is the specific case where all pairings besides $\Delta^0_{ba}, \Delta^c_{ba}$ are zero. Here, equation (78) describes the SC parameter for all values of $\boldsymbol{k}$. A critical point to our analysis' veracity in this case is the parameter ratio $\frac{\Delta^0_{ba}}{\Delta^c_{ba}}$ - for values $\left|\frac{\Delta^0_{ba}}{\Delta^c_{ba}}\right| \geq 2$ there exist points $\boldsymbol{k}_j$ in the BZ for which $\tilde{\Delta}(\boldsymbol{k}_j) = 0$ ((79)), for which equations (60) and (61) imply other possible gapless points. Our weak coupling assumption here therefore takes the form $\left|\frac{\Delta^0_{ba}}{\Delta^c_{ba}}\right| < 2$.

5 Conclusions

This work was an attempt to tackle topological superconductivity and its implications in low dimensions (1D and 2D), using a two pronged approach. On the one hand a more practical and experiment-oriented study of such a realized 1D system, and on the other hand a more theoretical approach to studying topological superconductivity in a new variation on a studied 2D system.

In the first part, a theoretical analysis of an experimental STM probe of a potential realization of 1D topological superconductivity was performed. This realization consisted of gated semiconducting (InAs) nanowires coated with a spattering of superconducting drops (Al), whose conductance was measured by the STM apparatus as the bias voltage was scanned. At first, the system was studied when not in a superconducting phase in order to lay the groundwork for study of its superconducting phase. An existing scheme for modeling the system as a DBTJ dubbed the simplified $\rho(E)$ model was utilized and was found to describe the broad strokes features of the measurements - Coulomb blockade dynamics due to substantial charging energy of the Al islands.

This simplified model, however, failed to account for the fine features or the measurements or to provide predictions for the system's behavior when in its superconducting phase. The underlying assumptions of the model were revisited and a new, refined $\rho(E)$ model was proposed, which accounts for the nontrivial energy structure of the DoS of the composing materials and of the tunneling coefficients, even accommodating superconductivity, and a numerical simulation of the model was written to accompany the analysis. Each of the possible causes for the fine features in the measurements was then studied separately. First, the effect of significant nontrivial nanowire DoS was deemed incompatible with even the broad features of the measurements as well as the fine features, and was therefore written off as a non-significant factor. Then, a more in-depth examination of the island-to-nanowire tunneling interface suggested an energy dependent tunneling coefficient due to an energy barrier over the sharp interface. To account for this effect a model of this interface and the resulting tunneling coefficient was suggested, agreeing nicely with the fine features of the measurement.

Finally, predictions on future measurements of superconducting and topologically superconducting phases were suggested, supported by measurements in the regular superconductivity case, including a prominent, replicating Majorana edge mode signature not at zero bias.

A natural next step would be to combine the effects mentioned above together, as they were only considered in isolation. First, a more rigorous study of the combined effect of nontrivial nanowire DoS and the tunneling matrix element is needed in order to understand why the predicted effects of nontrivial nanowire DoS are not seen in the measurements. It may corroborate or rule out our assumption that the suggested effect is "washed out" by the more powerful nontrivial tunneling coefficient effect. Second, studying the joint effect of both the tunneling coefficient and regular\topological superconductivity is of the highest order of importance in order to understand the fine features of future measurements in the experimental system.

The effects of temperature were neglected in our treatment under reasonable assumptions and accounted for in a roundabout way, but can actually be accounted for directly, albeit with increased numerical complexity. Comparing the differences between the full temperature-dependent calculations and ours and trying to find the difference in the data should prove enlightening.

In the second part, a theoretical study of a novel potential 2D realization of topological superconductivity was performed. First, a variation on the BHZ tight-binding model for a pseudo-spin Chern insulator was studied, culminating in the characterization of all its topological phases using a strong topological index - the

Chern number $\nu \in \mathbb{Z}$. A topological phase diagram was constructed using analytical means by examining the possible gapless points of the system, as the Chern number can only change after a gap closing and reopening, and verified numerically. Next, possible ways to introduce superconductivity to the model were considered, and a strictly intra-site form of superconductivity was chosen. The model was then recast into the BdG formalism, and a rich phase diagram using the Chern number ν was constructed, using the same previous method of pinpointing possible gapless points, and then verified numerically.

To further classify the topological phases of the system as well as understand its edge mode structure, the concept of weak topological phases and their corresponding weak topological indices was introduced. In contrast to the robust edge modes of strong topological phases, these phases exhibit "weak" edge modes along specific lines parallel to the BZ's symmetry axes. The indices can also be used to differentiate different strong topological phases.

The implementation of this concept in our system revolves around the Hamiltonian's properties at the high symmetry points in the BZ, which are the only possible gapless points in our system, and affords the definition of 4 weak topological indices $\nu_{x,0}, \nu_{x,\pi}, \nu_{y,0}, \nu_{y,\pi}$, 2 of which are redundant in phase characterization due to their connection with the Chern number ν. The indices were calculated explicitly, and a full topological phase diagram characterized by $\nu : \nu_{x,\pi}, \nu_{y,\pi}$ was found analytically. The exact relation between these indices and the edge modes of the corresponding topological phases was then highlighted and discussed. Lastly, the previous conclusions were generalized to the case of weak inter-site superconducting pairing.

A possible future direction of study would be to go beyond the weak SC pairing regime or study only intra-site superconductivity where our approach breaks down, in order to try and find topological phases unrealized in our system. Specifically, introducing p+ip superconductivity to our system should prove interesting, as it has been integrated into topologically trivial models to create rich topological phases. Another option to realize new phases would be to modify the Chern insulator model, which is the basis of our analysis. For example, making the t hopping anisotropic in amplitude would separate the phase lines corresponding to the $(0, \pi)$ and $(\pi, 0)$ gapless points, enriching the phase diagram further.

References

[1] Bernevig, B.A. and Hughes, T.L., 2013. *Topological insulators and topological superconductors.* Princeton university press.

[2] Hasan, M.Z. and Kane, C.L., 2010. *Colloquium: topological insulators.* Reviews of modern physics, 82(4), p.3045.

[3] Qi, X.L. and Zhang, S.C., 2011. *Topological insulators and superconductors.* Reviews of Modern Physics, 83(4), p.1057.

[4] Read, N. and Green, D., 2000. Paired states of fermions in two dimensions with breaking of parity and time-reversal symmetries and the fractional quantum Hall effect. *Physical Review B, 61*(15), p.10267.

[5] Kitaev, A.Y., 2001. Unpaired Majorana fermions in quantum wires. *Physics-Uspekhi, 44*(10S), p.131.

[6] Kitaev, A.Y., 2003. Fault-tolerant quantum computation by anyons. *Annals of Physics, 303*(1), pp.2-30.

[7] Nayak, C., Simon, S.H., Stern, A., Freedman, M. and Sarma, S.D., 2008. Non-Abelian anyons and topological quantum computation. *Reviews of Modern Physics, 80*(3), p.1083.

[8] Alicea, J., 2012. New directions in the pursuit of Majorana fermions in solid state systems. *Reports on progress in physics, 75*(7), p.076501.

[9] Lutchyn, R.M., Sau, J.D. and Sarma, S.D., 2010. Majorana fermions and a topological phase transition in semiconductor-superconductor heterostructures. *Physical Review Letters, 105*(7), p.077001.

[10] Oreg, Y., Refael, G. and von Oppen, F., 2010. Helical liquids and Majorana bound states in quantum wires. *Physical Review Letters, 105*(17), p.177002.

[11] Das, A., Ronen, Y., Most, Y., Oreg, Y., Heiblum, M. and Shtrikman, H., 2012. Zero-bias peaks and splitting in an Al–InAs nanowire topological superconductor as a signature of Majorana fermions. *Nature Physics, 8*(12), p.887.

[12] Mourik, V., Zuo, K., Frolov, S.M., Plissard, S.R., Bakkers, E.P. and Kouwenhoven, L.P., 2012. Signatures of Majorana fermions in hybrid superconductor-semiconductor nanowire devices. *Science, 336*(6084), pp.1003-1007.

[13] Karzig, T., Knapp, C., Lutchyn, R.M., Bonderson, P., Hastings, M.B., Nayak, C., Alicea, J., Flensberg, K., Plugge, S., Oreg, Y. and Marcus, C.M., 2017. Scalable designs for quasiparticle-poisoning-protected topological quantum computation with Majorana zero modes. *Physical Review B, 95*(23), p.235305.

[14] Plugge, S., Landau, L.A., Sela, E., Altland, A., Flensberg, K. and Egger, R., 2016. Roadmap to Majorana surface codes. *Physical Review B, 94*(17), p.174514.

[15] Seroussi, I., Berg, E. and Oreg, Y., 2014. Topological superconducting phases of weakly coupled quantum wires. *Physical Review B, 89*(10), p.104523.

[16] Sau, J.D., Lutchyn, R.M., Tewari, S. and Sarma, S.D., 2010. Generic new platform for topological quantum computation using semiconductor heterostructures. *Physical review letters, 104*(4), p.040502.

[17] Fu, L. and Kane, C.L., 2008. Superconducting proximity effect and Majorana fermions at the surface of a topological insulator. *Physical review letters, 100*(9), p.096407.

[18] Asahi, D. and Nagaosa, N., 2012. Topological indices, defects, and Majorana fermions in chiral superconductors. *Physical Review B, 86*(10), p.100504.

[19] Schnyder, A.P., Ryu, S., Furusaki, A. and Ludwig, A.W., 2009, May. Classification of topological insulators and superconductors. In *AIP Conference Proceedings* (Vol. 1134, No. 1, pp. 10-21). AIP.

[20] Ryu, S., Schnyder, A.P., Furusaki, A. and Ludwig, A.W., 2010. Topological insulators and superconductors: tenfold way and dimensional hierarchy. *New Journal of Physics, 12*(6), p.065010.

[21] Fu, L. and Kane, C.L., 2007. Topological insulators with inversion symmetry. *Physical Review B, 76*(4), p.045302.

[22] Mullen, K., Gefen, Y. and Ben-Jacob, E., 1988. The dynamics of mesoscopic normal tunnel junctions. *Physica B: Condensed Matter, 152*(1-2), pp.172-185.

[23] Amman, M., Wilkins, R., Ben-Jacob, E., Maker, P.D. and Jaklevic, R.C., 1991. Analytic solution for the current-voltage characteristic of two mesoscopic tunnel junctions coupled in series. *Physical Review B, 43*(1), p.1146.

[24] Amman, M., Mullen, K. and Ben-Jacob, E., 1989. The charge-effect transistor. *Journal of Applied Physics, 65*(1), pp.339-346.

[25] Bardeen, J., 1961. Tunnelling from a many-particle point of view. *Physical Review Letters, 6*(2), p.57.

[26] Reiner, J, 2018. Scanning Tunneling Microscopy Study of Electronic Behavior in Semiconducting Nanowires (Doctoral dissertation, Weizmann Institute of Science, Israel).

[27] Averin, D.V. and Likharev, K.K., 1991. Single electronics: A correlated transfer of single electrons and Cooper pairs in systems of small tunnel junctions. *Modern Problems in Condensed Matter Sciences, Vol. 30*, pp. 173-271.

[28] Hanna, A.E. and Tinkham, M., 1991. Variation of the Coulomb staircase in a two-junction system by fractional electron charge. *Physical Review B, 44*(11), p.5919.

[29] Millo, O., Katz, D., Cao, Y. and Banin, U., 2000. Scanning tunneling spectroscopy of InAs nanocrystal quantum dots. *Physical Review B, 61*(24), p.16773.

[30] Tinkham, M., 2004. *Introduction to superconductivity*, p.70. Courier Corporation.

[31] Cohen-Tannoudji, C., Diu, B., Laloë, F., et al. 1996. *Quantum mechanics.* Wiley. pp. 231–233.

[32] Tinkham, M., Hergenrother, J.M. and Lu, J.G., 1995. Temperature dependence of even-odd electron-number effects in the single-electron transistor with a superconducting island. *Physical Review B, 51*(18), p.12649.

[33] Tuominen, M.T., Hergenrother, J.M., Tighe, T.S. and Tinkham, M., 1993. Even-odd electron number effects in a small superconducting island: Magnetic-field dependence. *Physical Review B, 47*(17), p.11599.

[34] Bernevig, B.A., Hughes, T.L. and Zhang, S.C., 2006. Quantum spin Hall effect and topological phase transition in HgTe quantum wells. *Science, 314*(5806), pp.1757-1761.

[35] Altland, A. and Simons, B.D., 2010. Condensed matter field theory. Cambridge University Press.

[36] De Lisle, J., De, S., Alba, E., Bullivant, A., Garcia-Ripoll, J.J., Lahtinen, V. and Pachos, J.K., 2014. Detection of Chern numbers and entanglement in topological two-species systems through subsystem winding numbers. *New Journal of Physics, 16*(8), p.083022.

[37] Economou, E.N., 1983. *Green's functions in quantum physics* (Vol. 3), 12.58. New York: Springer.

6 Acknowledgments

First and foremost, I would like to express my humble gratitude to my advisors, Prof. Yuval Oreg and Prof. Ady Stern. Thank you for always sharing and amazingly elucidating your knowledge, understanding and intuition, for having the patience and the willingness to dedicate your time to helping me out with things both large and small, but above all for being amazing human beings. Our joint meetings always stirred in me a mix of understanding, confusion, a sense of discovery and good spirits, always pushing forward in the end, and I loved every minute of them. Even though the road was laced with frustration and we finished the project far from where we thought we would when we started, it was still a journey I greatly enjoyed, and it was a pleasure to work with you.

I wish to thank my collaborators on the nanowire front, Dr. Jonathan Reiner and Dr. Haim Beidenkopf. Jonathan, you were a blast to work with, a formidable partner for speculation and debate and a wise proponent of the experimentalist's way of doing things, which I found to be invaluable. Haim, thank you for always being there to restore focus and clarity to our efforts and to drop words of wisdom.

I also wish to thank Eyal Leviathan, for multiple illuminating discussions on a wide variety of physics topics but mostly for being an awesome office-mate, Omri Lesser, for your insight in constructing the numerical simulation for the second part of the thesis, and the rest of the Condensed Matter Theory department, for always being up for discussion about related and unrelated topics and for the weekly hilarious Hummus Thursdays.

Lastly, I would like to thank Tom Koren, Ron Melcer, Omer Kneller, Maya Weiss, Amir Sharon, Moran Netser, Jonathan Mushkin and Zohar Nowick, as well as the rest of the regular Parliament crowd. From lunch breaks to coffee breaks, it was always a pleasure discussing everything from physics to nonsense with you. You guys gave this year a great feeling of fun and camaraderie which I will always cherish.

7 Appendices

7.1 Model for InAs Nanowire DoS

Naively, one would expect a 1D dispersion which is a series of van-Hove singularities:

$$\rho_{\text{InAs}} \propto \rho^0_{\text{InAs}} \sum_{n=0}^{\infty} \frac{1}{\sqrt{E - E_n}} \Theta\left(E - E_n\right)$$

Where E_n describes the sub-band energy level spacing (the nanowire is assumed to be much longer than its width, therefore the longitudinal quantization is ~continuous and can be integrated out, in contrast to the transverse direction quantization):

$$E_n = E_0 + n\delta E$$

And E_0 is the onset the conduction band, δE is the sub-band spacing. A fit to the experimental measurement (Figure (3)) gives:

$$E_0 \approx -100meV$$

$$\delta E \approx 20meV$$

However, when taking into account hybridization of the InAs with the Al, these features must be smeared, and so this must be taken into consideration for $\rho_{\text{InAs}}\left(E\right)$.

Starting from scratch, using Dyson's equation we can write the corresponding Green's function as [37]:

$$G_{nn}\left(E\right) = \frac{1}{E - E_n - \Sigma_{nn}\left(E\right)}$$

Where Σ is the self-energy term, which we approximate as $\sim i\Gamma$ for all relevant energies as we assume the metal is coupled in the same fashion to all nanowire states, and we are only interested in the diagonal terms as we will soon take a trace to find the DoS. Then:

$$\rho\left(E\right) \propto \text{Tr}\left(\Im\left(G_{nn}\left(E + i0\right)\right)\right) = \sum_n \Im\left(G_{nn}\left(E + i0\right)\right) = \sum_n \Im\left(\frac{1}{E - E_n - i\Gamma}\right) = \sum_n \frac{\Gamma}{\left(E - E_n\right)^2 + \Gamma^2}$$

This indeed produces a smeared density of states by a Lorentzian factor - something that should give separated levels in the $\Gamma \to 0$ limit:

$$\rho\left(E\right) = \sum_n \delta\left(E - E_n\right)$$

Which it does, as:

$$\delta\left(\epsilon\right) = \lim_{\Gamma \to 0} \frac{1}{\pi} \frac{\Gamma}{\epsilon^2 + \Gamma^2}$$

For our problem, we take the energies as:

$$E^l_k = \frac{\hbar^2 k^2}{2m} + E_0 + \underbrace{\delta}_{\text{subband energy spacing}} l$$

Where k is the band quantization and l is the sub-band quantization. Then, assuming k is dense (L is the nanowire length):

$$\begin{aligned}\rho(E) &= \sum_{k,l} \frac{1}{\pi} \frac{\Gamma}{\left(E - E_k^l\right)^2 + \Gamma^2} \\ &= \frac{1}{\pi\Gamma} \frac{L}{2\pi} \sum_{l=0}^{\infty} \int_{-\infty}^{\infty} dk \frac{1}{\left(\frac{\frac{\hbar^2 k^2}{2m}}{\Gamma} - \frac{E-(E_0+\delta l)}{\Gamma}\right)^2 + 1}\end{aligned}$$

The integration can be performed analytically, yielding:

$$\rho(E) = \frac{L}{2\pi} \frac{1}{\sqrt{\Gamma}} \frac{\sqrt{m}}{\hbar} \sum_{l=0}^{\infty} \frac{\sqrt{\frac{E-(E_0+\delta l)}{\Gamma} + \sqrt{\left(\frac{E-(E_0+\delta l)}{\Gamma}\right)^2 + 1}}}{\sqrt{\left(\frac{E-(E_0+\delta l)}{\Gamma}\right)^2 + 1}}$$

This allows us control of an additional parameter, the broadening parameter Γ, which is needed fit our model to the measured InAs density of states.

An example for the best fit for the conductance with only nontrivial $\rho_{\text{InAs}}(E)$ is brought below. It required lowering the threshold of the onset of the conductance band E_0 to ~ -500 meV in contrast with our fitting results, and still creates distinct "wiggles" that do not appear in the measurement and asymmetry between positive and negative biases.

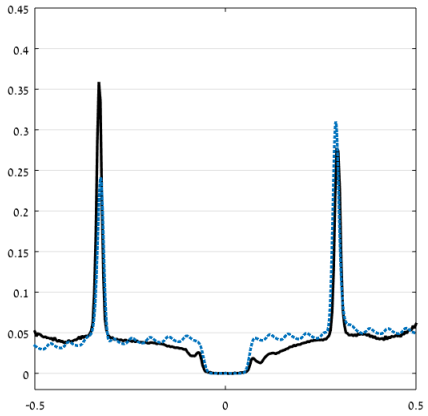

Figure 18: Best fit (dashed blue line) for the conductance measurement (black line) for only nontrivial $\rho_{\text{InAs}}(E)$.

7.2 Refined $\rho(E)$ Model Numerical Simulation Protocol

A MATLAB script was written, taking as input the model variables C_1, C_2 and the functional forms of all density of state functions and tunneling elements, in turn evaluating all $\Gamma_j\left(\Delta E_j^{\pm}\right)$ numerically and employing the fact that $\sigma(N,V)$ is generally nonzero only for a few adjacent values of N to calculate $\sigma(N,V)$ to finite (but as great as required) accuracy using equations (10), (21), (22). This allows the calculation of the current using equation (15), which is then numerically differentiated to find the conductance.

Given parametrized models of all required functional forms, an additional script implemented a fitting

algorithm to the experimentally measured conductance in order to find the best fit values of the parameters (e.g. in the nontrivial $T_1(E)$ case, all DoS are set as constant with a single parameter for magnitude, and the $T_1(E)$ fitting parameters V_0 and Φ).

7.3 Explicit Construction of a Majorana Fermion at a Weak Phase Boundary

We will show the Majorana residing at a boundary parallel to the x axis with $k_x = \pi$ between the weak topological phase $0:11$ and the trivial phase $0:00$ (the treatment for the ones at $k_x = 0$,$k_y = 0, \pi$ is similar). Recalling equations (73),(74):

$$\begin{aligned} s_{\mathbf{\Gamma}_i} &= \text{sign}\left(d_z\left(\mathbf{\Gamma}_i\right)^2 - \left(\mu^2 + \Delta^2\right)\right) \\ &= \begin{cases} 1 & \sqrt{\mu^2+\Delta^2} < \left|d_z\left(\mathbf{\Gamma}_i\right)\right| \\ -1 & \sqrt{\mu^2+\Delta^2} > \left|d_z\left(\mathbf{\Gamma}_i\right)\right| \end{cases} \end{aligned}$$

We take the trivial phase $0:00$ with (see Table (1)):

$$\begin{matrix} s_{(0,\pi)} & s_{(\pi,\pi)} \\ s_{(0,0)} & s_{(\pi,0)} \end{matrix} = \begin{matrix} + & + \\ + & + \end{matrix} \iff |\Delta| < \left|d_z(0,0)\right|, \left|d_z(0,\pi)\right|, \left|d_z(\pi,0)\right|, \left|d_z(\pi,\pi)\right|$$

And the weak topological phase $0:11$ with:

$$\begin{matrix} s_{(0,\pi)} & s_{(\pi,\pi)} \\ s_{(0,0)} & s_{(\pi,0)} \end{matrix} = \begin{matrix} - & + \\ + & - \end{matrix} \iff |\Delta| < \left|d_z(0,0)\right|, \left|d_z(\pi,\pi)\right|, |\Delta| > \left|d_z(0,\pi)\right|, \left|d_z(\pi,0)\right|$$

Next, we can set a phase boundary parallel to the x axis (at $y = 0$ without loss of generality) by making the SC parameter Δ a function of y which places the system into the two different phases at $y < 0$ and $y > 0$:

$$\Delta \to \Delta(y) = \begin{cases} > \max\left\{\left|d_z(0,\pi)\right|, \left|d_z(\pi,0)\right|\right\} & y > 0 \\ < \min\left\{\left|d_z(0,\pi)\right|, \left|d_z(\pi,0)\right|\right\} & y < 0 \end{cases}$$

Next we write the effective real space BdG Hamiltonian, as a function of y around $k_y = 0$ (keeping k_y terms up to linear order) and at $k_x = \pi$:

$$H_{\text{BdG}}(\pi, y) = \left(A\left(-i\partial_y\right)\sigma_y + d_z(\pi,0)\,\sigma_z\right)\tau_z - \Delta(y)\,\sigma_y\tau_y$$

We are looking for zero energy modes χ, and so we must satisfy $H_{\text{BdG}}\chi = 0$ for them. The eigenvalue equation becomes:

$$\left(\left(A\left(-i\partial_y\right)\sigma_y + d_z(\pi,0)\,\sigma_z\right)\tau_z - \Delta(y)\,\sigma_y\tau_y\right)\chi = 0$$

We can multiply the entire equation by $\tau_z\sigma_y$ from the left and get:

$$\left(-A\partial_y + d_z(\{0,\pi\},0)\,\sigma_x + \Delta(y)\,\tau_x\right)\chi = 0$$

We look for a solution of the form (u is a vector in τ subspace, v is a vector in σ subspace)

$$\chi_{\eta,\upsilon} \propto e^{\lambda_{\eta,\upsilon} y}\boldsymbol{u}_\eta \boldsymbol{v}_\upsilon$$

Where $u_\pm, v_\pm$ are eigenvectors of τ_x, σ_x with eigenvalues ± 1. Plugging this in we get the scalar equation for $\lambda_{\eta,\upsilon}$:

$$\lambda_{\eta,\upsilon} = A^{-1}\left(\upsilon d_z\left(\pi,0\right) + \eta\Delta\left(y\right)\right)$$

which we must solve for $y > 0$ and $y < 0$ separately. The wavefunction must be regular for $y \to \pm\infty$, which means $\text{sign}\left(\lambda\right) = \begin{cases} -1 & y > 0 \\ 1 & y < 0 \end{cases}$. The first requirement sets $\eta = -1$, and the second one then sets $\upsilon = -\text{sign}\left(d_z\left(\pi,0\right)\right)$, meaning only a single pair η, υ gives a valid solution. This solution is in fact (α is the normalization factor, set up to global phase)

$$\begin{aligned}
\chi_{-1,\upsilon}\left(k_x = \pi, y\right) &= \alpha e^{\lambda(y)y}\frac{1}{2}\begin{pmatrix} 1 \\ -1 \end{pmatrix}_\tau \begin{pmatrix} 1 \\ \upsilon \end{pmatrix}_\sigma \\
&= \alpha e^{\lambda(y)y}\frac{1}{2}\begin{pmatrix} 1 \\ \upsilon \\ -1 \\ -\upsilon \end{pmatrix} \\
&= \alpha e^{\lambda(y)y}\frac{1}{2}\left(a_{k_x,0} + \upsilon b_{k_x,0} - \left(a^\dagger_{-k_x,0} + \upsilon b^\dagger_{-k_x,0}\right)\right) \\
&= \alpha e^{\lambda(y)y}\frac{1}{2}\left(\left(a_{k_x,0} - a^\dagger_{-k_x,0}\right) + \upsilon\left(b_{k_x,0} - b^\dagger_{-k_x,0}\right)\right)
\end{aligned}$$

This is indeed a Majorana (when setting the global phase factor as i), as a Majorana in momentum space $\gamma_{\boldsymbol{k}}$ satisfies $\gamma^\dagger_{-\boldsymbol{k}} = \gamma_{\boldsymbol{k}}$:

$$\begin{aligned}
\chi^\dagger_{-1,\upsilon}\left(-k_x = -\pi, y\right) &= \alpha e^{\lambda(y)y}\frac{(-i)}{2}\left(\left(a^\dagger_{-k_x,0} - a_{k_x,0}\right) + \upsilon\left(b^\dagger_{-k_x,0} - b_{k_x,0}\right)\right) \\
&= \alpha e^{\lambda(y)y}\frac{i}{2}\left(\left(a_{k_x,0} - a^\dagger_{-k_x,0}\right) + \upsilon\left(b_{k_x,0} - b^\dagger_{-k_x,0}\right)\right) \\
&= \chi_{-1,\upsilon}\left(k_x = \pi, y\right)
\end{aligned}$$

As we wanted to show. Note that also in the BZ, π and $-\pi$ are identified as the same point, and therefore also:

$$\chi^\dagger_{-1,\upsilon}\left(\pi, y\right) = \chi_{-1,\upsilon}\left(\pi, y\right)$$